

# Gabor Fields: Orientation-Selective Level-of-Detail for Volume Rendering

JORGE CONDOR\*, USI Lugano, Switzerland  
 NICOLAI HERMANN\*, USI Lugano, Switzerland  
 MEHMET ATA YURTSEVER, USI Lugano, Switzerland  
 PIOTR DIDYK, USI Lugano, Switzerland

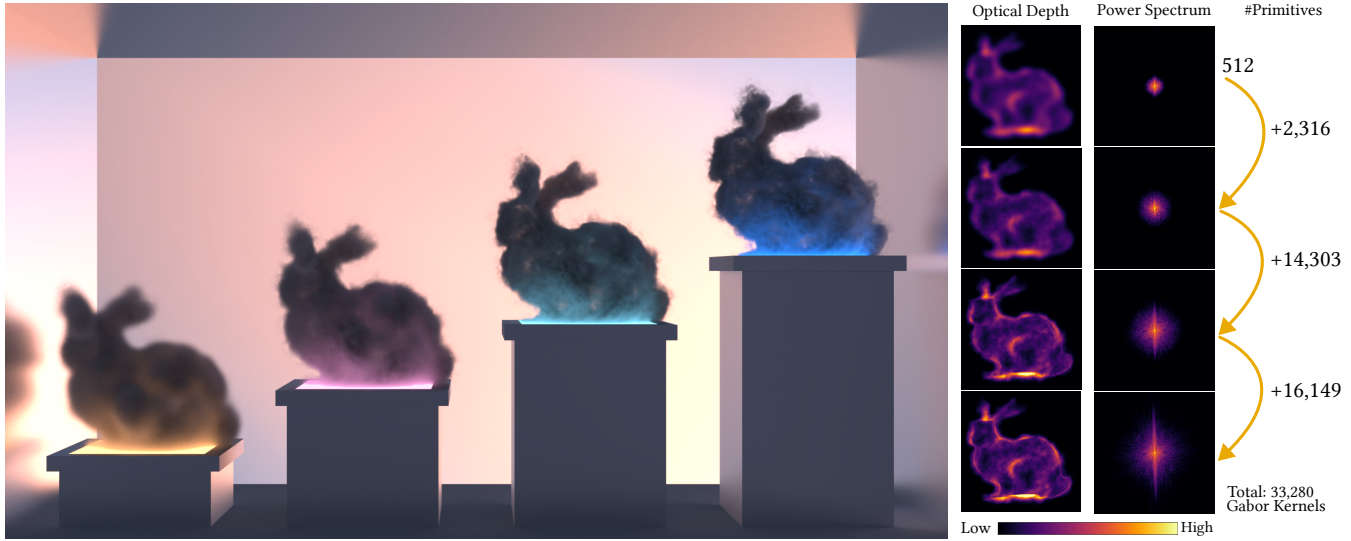


Fig. 1. Example level-of-detail decomposition of our Gabor Fields, a new volumetric density field representation using primitive Gabor kernels. The frequency- and orientation-selectivity of the representation enables continuous control over level of detail, reduced rendering time, and a trade-off between variance and bias for performance when sample cost is critical. Here, we show four levels obtained by masking particle collections from the highest-quality asset at render time. (Volumetric BUNNY from the OpenVDB database [DreamWorksAnimation 2023])

Gaussian-based representations have enabled efficient physically-based volume rendering at a fraction of the memory cost of regular, discrete, voxel-based distributions. However, several remaining issues hamper their widespread use. One of the advantages of classic voxel grids is the ease of constructing hierarchical representations by either storing volumetric mipmaps or selectively pruning branches of an already hierarchical voxel grid. Such strategies reduce rendering time and eliminate aliasing when lower levels of detail are required. Constructing similar strategies for Gaussian-based volumes is not trivial. Straightforward solutions, such as prefiltering or computing mipmap-style representations, lead to increased memory requirements or expensive re-fitting of each level separately. Additionally, such solutions do not guarantee a smooth transition between different hierarchy levels. To address these limitations, we propose Gabor Fields, an orientation-selective mixture of Gabor kernels that enables continuous frequency filtering at no cost. The frequency content of the asset is reduced by selectively pruning primitives, directly benefiting rendering performance. Beyond filtering, we demonstrate that stochastically sampling from different frequencies and orientations at each ray recursion enables masking substantial portions of the volume, accelerating ray traversal time in single- and multiple-scattering settings. Furthermore, inspired by procedural volumes,

we present an application for efficient design and rendering of procedural clouds as Gabor-noise-modulated Gaussians.

## 1 Introduction

High-quality volumetric representations are central for many applications in computer graphics. They are widely used, especially when obtaining or using explicit representations is difficult or prohibitively expensive. Examples include modeling and simulation of particle aggregates [Meng et al. 2015; Moon et al. 2007], clouds [Kallweit et al. 2017], foliage [Loubet and Neyret 2017; Neyret 1998], cloth [Schröder et al. 2011; Zhao et al. 2011] and hair [Petrovic et al. 2005]. Most of the above methods use discrete density distributions as their primitive model, organized in 3D voxel grids that can be dense, adaptive [Museth 2013a] or partly implicit [Kim et al. 2024]. A significant drawback of these methods is their poor memory scalability and the need to use stochastic methods for efficient rendering with physically-based path tracers [Novák et al. 2018], which limits the potential of volumetric rendering techniques.

In recent years, Lagrangian-style particle methods have become the volumetric representation of choice underpinning applications including radiance field reconstructions [Kerbl et al. 2023; Lassner and Zollhofer 2021; Wu et al. 2024], simultaneous localization and mapping (SLAM) [Keetha et al. 2024], mesh extraction [Guédon and Lepetit 2024], or fast tomographic rendering [Gao et al. 2025].

\*Both authors contributed equally to this research.

Authors' Contact Information: Jorge Condor, jorge.condor@usi.ch, USI Lugano, Lugano, Ticino, Switzerland; Nicolai Hermann, nicolai.hermann@usi.ch, USI Lugano, Lugano, Switzerland; Mehmet Ata Yurtsever, ata.yurtsever@usi.ch, USI Lugano, Lugano, Switzerland; Piotr Didyk, piotr.didyk@usi.ch, USI Lugano, Lugano, Switzerland.

Inspired by these developments, Condor et al. [2025] proposed a technique to efficiently model and render kernel mixture models bounded by volumetric primitives. The method replaced discrete volumetric density distributions with continuous ones, providing substantial memory and speed improvements over traditional voxel grids. The generality of this technique enables both path tracing and radiance field rendering, offering multiple advantages over previous rasterized frameworks, such as support for complex camera models, the ability to trace secondary rays to compute relighting, shadowing, scattering, and analytic transmittance integrals. However, the approach has several limitations. The modeling power of the Gaussian kernels is limited, and the regression scales poorly. Moreover, Gaussian volumetric primitives are not directly compatible with level-of-detail (LOD) strategies. The analogous approach to downsampling voxel grids would require convolving primitives with a low-pass filter, for example, another Gaussian, producing new Gaussian primitives with larger spatial supports. Such a representation would have the same complexity yet slower rendering time. While aggregating primitives after filtering is possible, it would require energy-based optimizations or re-fitting of the asset.

To address these limitations, we draw inspiration from steerable pyramid decompositions [Simoncelli and Freeman 1995; Simoncelli et al. 1992] and propose a hierarchical volumetric primitive representation based on mixtures of Gaussian and Gabor kernels. Gabor kernels, harmonically modulated Gaussians, have a frequency-domain representation consisting of symmetric, opposed Gaussians centered around their peak modulation frequency (see Figure 3). This spectral localization makes them ideal for constructing a spectrally aware volumetric representation in which filtering specific spatial frequency bands corresponds to removing certain kernels. This enables a simple LOD strategy that does not require additional memory or create discontinuities between levels. These properties make LOD both natural and efficient, similar to a continuous Laplacian pyramid but with orientation selectivity. We support this representation with analytically derived line integrals for the Gabor kernels and a novel hierarchical regression scheme. In addition, we propose an efficient stochastic rendering approach that leverages the unique properties of the representation to drastically reduce cost per sample in brute-force multiple-scattering path tracing settings. Furthermore, Gabor kernels are orientation-selective. They model residuals only in specific frequencies and orientations, contributing negligibly in others. We demonstrate, for the first time, that this property can be effectively leveraged to improve rendering time by selectively masking particles that do not contribute significantly to a given ray. Our main contributions can be summarized as:

- a novel frequency- and orientation-selective volumetric density representation,
- analytic line integral and sampling solutions for tomographic rendering, single and multiple scattering, forward and inverse path tracing,
- a regression scheme for distilling 3D density fields into Gabor Fields,
- strategies leveraging the new representation to accelerate physically based rendering,

- applications to efficient LOD, motion blur, and noise-inspired procedural asset generation.

## 2 Related Work

*Monte Carlo Volume Rendering.* Simulating light transport in participating media has been a longstanding area of research in computer graphics, typically requiring solutions to the radiative transfer equation [Chandrasekhar 1960]. Due to the dimensionality of the integral, it is most often estimated stochastically using Monte Carlo approaches; an excellent survey can be found in [Novák et al. 2018]. Some popular approaches include ray marching [Kettunen et al. 2021; Tuy and Tuy 1984], also used transversally in many implicit radiance field rendering applications [Mildenhall et al. 2020; Müller et al. 2022]; and null-scattering estimators [Woodcock 1965], either fully analogical or with partial closed-form estimation and sample reweighting (i.e. control variates) [Crespo et al. 2021; Novák et al. 2014; Szirmay-Kalos et al. 2017], or leveraging power-series expansions [Georgiev et al. 2019]. Representing heterogeneous media typically involves voxel grids due to their simplicity and support for hierarchical acceleration structures [Museth 2013a, 2021a], though these become memory-intensive when high amounts of detail are required.

*Physically Based Volume Rendering with Volumetric Primitives.* Alternatives to voxel grids have been studied in the past. Sparse representations, such as collections of isotropic volumes used in particle physics [Brown and Martin 2003; Max 1979], suffer from the limited modelling power of isotropic primitives. Recent similar efforts in vision and graphics do not fully leverage the advantages of closed-form integration [Knoll et al. 2021; Lassner and Zollhofer 2021] and do not support scattering. Other alternatives include hierarchical grids [Fong et al. 2017], implicit MLP mixtures [Lombardi et al. 2021; Reiser et al. 2021] and sparse feature grids [Müller et al. 2022]; these trade-off quality, speed or compression, but overall do not provide a completely rounded solution. More recently, and inspired by primitive-based radiance field efforts [Kerbl et al. 2023], anisotropic ellipsoid-bounded kernel mixture models [Condor et al. 2025] were proposed, providing a compact, fast and relatively high quality alternative. Our work is directly based on these, where our novel hierarchical, spectrally-bounded regression and the introduction of a new kernel (anisotropic Gabor) improves on some of the limitations of the approach, namely, regression quality for low mixture complexities, rendering speed and efficient support of LODs.

*Gabor Kernels and Noise in Rendering.* A Gabor kernel combines a Gaussian envelope with a sinusoidal wave. Its sensitivity to frequency and orientation is widely exploited in image processing and computer vision. Gabor kernels are commonly used in the study and modeling of human visual perception, as they can mimic the human visual system's sensitivity to specific orientations, spatial frequencies, and locations within the visual field [Marcelja 1980]. They have been successfully used to define procedural noise and texture synthesis methods [Galerne et al. 2012; Lagae et al. 2009], offering a compact and resolution-independent approach to generate structured randomness in textures and materials which avoids

storage and bandwidth requirements of image-based textures, and support infinite detail through frequency-aware evaluation. In the particular case of volume modeling and rendering, procedural noise is ubiquitous, as it is common for games and VFX production to allow artists or fluid dynamics solvers to create a guide distribution (i.e., metaballs or constant density ellipsoids [Wrenninge et al. 2011]) and layer noise on top to create compact and visually appealing assets [Fajardo et al. 2023]. Our work bridges the gap between procedural and explicitly generated assets through a unified framework. It enables us to construct extremely compact multi-resolution volumetric fields. Assets can be produced in a forward (procedural noise generation) or inverse manner (regression of already existing discrete density fields), and both can be efficiently rendered leveraging closed-form transmittance integrals, which we pioneer for Gabor kernels in this work.

*Level of Detail.* The concept of LOD is crucial for optimizing rendering costs and providing prefiltered versions of assets to prevent aliasing. LOD is most commonly associated with meshes, where the geometric complexity of rendered objects is adjusted according to their size in the image space [Luebke et al. 2002]. More similar to our approach, MIP mapping [Crow 1984] is a standard LOD technique for textures, where multiple prefiltered versions of textures, so-called pyramids, are stored, allowing for quick access to the appropriate level based on the texture’s screen-space footprint during rendering. The concept of hierarchical representation has also been applied to volumes. One of the pioneering methods for pyramidal volume representation, introduced by Laur and Hanrahan [Laur and Hanrahan 1991], was designed for efficient rendering based on the viewer’s location. Building on these ideas, Weiler et al. [2000] proposed an approach for volumes that ensures consistent interpolation between different resolution levels. Additionally, while not always explicitly, more recent volumetric representations, such as [Museth 2013b, 2021b], also provide a hierarchical representation. In contrast to these methods, our approach does not rely on a discrete volume representation. Instead, we represent the volume using implicit functions, specifically Gabor and Gaussian kernels. Closer to our work are wavelet-based hierarchical representations [Guthe et al. 2002]. Compared to this approach, our method offers a more expressive representation due to the flexibility of the kernels we use and analytical transmittance integrals, which are critical for efficient volumetric rendering.

When considering volume rendering, and similarly to regular textures, Gaussian pyramids are constructed in the form of Mipmaps (explicitly storing box-filtered copies of the asset at octaves) or adaptive voxel grids (early pruning of the traversal towards leaf nodes to cut query time). These methods rely on increased storage or decreased performance at full resolution to enable a static decomposition of the asset that saves performance when rendering at larger distances or smaller objects.

On the other hand, LOD for primitive-based volumes has been left largely unexplored until very recently. In the context of Gaussian Splatting, work has focused on Gaussian-pyramid like decompositions: training scenes at different scales, then proposing solutions to online switching between the different levels to maximize performance while minimizing artifacts during rendering [Windisch et al.

Table 1. Important variables used in the paper with their symbols.

Variable Name	Symbol
$\kappa$	Extinction Field
$\alpha$	Kernel Weight
$K_i$	Kernel
$\tau$	Optical Depth
$T$	Transmittance
$L$	In-scattered Radiance
$\sigma$	Standard Deviation
$\mu$	Kernel Mean
$\vec{\omega}$	Frequency and Orientation of the Gabor Modulation
$f_0$	Peak Frequency of the Gabor Modulation
$\Sigma$	Covariance Matrix
$W$	Whitening Matrix
$\vec{k}_W$	Frequency and Orientation in Whitened Space

2025]. If explicit storage is unfeasible due to the scale of the asset, chunking systems have been proposed [Kerbl et al. 2024], as well as streaming from global memory and implicit encoding of Gaussian parameters [Yang et al. 2025]. Similarly, different texturing alternatives have been proposed in order to compress the representation (via providing higher modelling power per primitive) [Chao et al. 2025], but so far it’s unproven whether the simple, learned textures can be safely filtered to provide LOD tools.

In contrast, we propose the first pure primitive-based volumetric model that can naturally decompose not only into different frequency bands, but that is also orientation-selective. This structure maximizes rendering speed and compression, as we do not need to further compute or store new pyramid levels to provide LOD, but rather simply mask out parts of the same asset to naturally obtain a continuous representation, spectrally-wise.

### 3 Background - Primitive Volume Rendering

Here we summarize how to perform physically-based volume rendering with *volumetric primitives* [Condor et al. 2025]. We further compiled a table of the most important variables for reference in Table 1. Each primitive defines a localized region of matter characterized by a density kernel  $K_i(\mathbf{x})$ , weight  $\alpha_i$ , emission, and phase function (the latter two omitted here for conciseness). Each kernel has limited support, being bounded by an ellipsoid with a primary axis radius of  $3\sigma$ , which in practice and for efficiency reasons, is approximated by a triangle mesh. The extinction field at any point  $\mathbf{x}$  is expressed as the sum over contributing primitives:

$$\kappa_t = \sum_{i=1}^N \alpha_i K_i(\mathbf{x}) \quad (1)$$

where  $N$  is the number of primitives influencing  $\mathbf{x}$ . For an arbitrary ray  $r = \mathbf{x}_0 + \vec{v} \cdot t$ , each primitive’s contribution to the optical depth along a ray segment  $[a, b]$  is given by

$$\tau_i(\mathbf{x}_a, \mathbf{x}_b) = \alpha_i \int_a^b K_i(\mathbf{x}_t) dt \quad (2)$$

Using an exponential decay model, the total transmittance  $T$  through the segment becomes

$$T(\mathbf{x}_a, \mathbf{x}_b) = \exp \left( - \sum_{i=1}^N \tau_i(\mathbf{x}_a, \mathbf{x}_b) \right), \quad (3)$$

*Segment-Based Radiative Transfer.* To evaluate radiance, the ray is partitioned into segments, determined by entry and exit points of the primitives. Radiance is computed as the sum of each segment's contribution, weighted by the accumulated transmittance:

$$L(\mathbf{x}_0, \mathbf{x}_M, \vec{v}) = \sum_{k=1}^M T_{k-1}(\mathbf{x}_0, \mathbf{x}_k) L_k(\mathbf{x}_{k-1}, \mathbf{x}_k, \vec{v}), \quad (4)$$

where  $L_k$  denotes the integrated in-scattered radiance within segment  $k$ , and  $T_{k-1}$  is the cumulative transmittance up to segment  $k$ . Sampling the interaction distance along the ray is achieved via inversion of the cumulative density function along the ray, for a given random sample  $\xi \in (0, 1)$ :

$$\log(1 - \xi) = - \sum_i^N \tau_i(\mathbf{x}_0, \mathbf{x}_i). \quad (5)$$

This allows for efficient sampling strategies via root-finding (Newton-Raphson, bisection) or closed-form inversion, depending on the choice of kernels. For dense scenes, uniform sampling within segments offers a bias-performance trade-off that remains effective in practice.

## 4 Our method

### 4.1 Motivation

As discussed in Section 1, Gaussian primitives are not directly compatible with practical LOD strategies due to their spectral properties. Their power spectrum spans all frequencies centered at the origin. We visualize this in Figure 2. In essence, analytically filtering Gaussians to create LOD levels creates a new asset that retains the same number of Gaussians with larger spatial support. Consequently, this method does not yield any performance improvements. Pruning Gaussians based on their size is not a viable solution, as even small Gaussians carry important low-frequency information. Removing them results in artifacts at the coarser levels. An even more costly option would be to refit the pre-filtered asset using a smaller set of Gaussians. This would require solving multiple expensive optimization problems and would have higher memory requirements. Furthermore, interpolation between levels could introduce artifacts if the levels are not refitted jointly.

Our first insight is that, ideally, an effective primitive volume LOD strategy should be constructed like a Laplacian pyramid. A single asset could be decomposed into different LODs by simply removing a subset of primitives, allowing regression in a single pass, and continuous filtering during rendering, at no extra memory cost. This requires a kernel that, in the frequency domain, solely exists within specific frequency bands, effectively modelling a residual between the current and previous levels. This is where harmonic-modulated kernels come into play. In particular, we propose using an adaptation of the Gabor kernel [Lagae et al. 2009]. We extend

the kernel by making it anisotropic, deriving closed-form line integrals for arbitrary segments, and a novel optimization scheme to regress volumetric density fields as mixtures of the kernel. We will then introduce several new strategies to leverage this volumetric representation to further accelerate rendering time in practical scenarios.

### 4.2 The 3D Anisotropic Gabor Kernel

Our 3D anisotropic Gabor kernel has the form

$$g(\mathbf{x}; \mu, \Sigma, \vec{\omega}) = \frac{1}{\sqrt{8\pi^3 |\Sigma|}} e^{-\frac{1}{2}(\mathbf{x}-\mu)^T \Sigma^{-1}(\mathbf{x}-\mu)} \cos(\vec{\omega}^T(\mathbf{x}-\mu)) \quad (6)$$

with  $S$  the diagonal scale matrix (principal axis standard deviations) and rotation matrix  $R$  of the Gaussian. Together they form a factorization of the covariance matrix  $\Sigma = RSS^T R^T$  [Kerbl et al. 2023]; and  $\omega$  being the orientation and magnitude of our planar wave modulation. In practice, we model the modulation  $\vec{\omega}$  using a scalar  $\omega$  and fix the orientation to be diagonal as  $\vec{\omega} = RS^{-1}(\omega, \omega, \omega)^T$ , making it relative to its envelope. This reduces the parameter count and simplifies the optimization. Our Gabor formulation is slightly different from the Gabor kernels typically used in Gaussian Textures [Galerne et al. 2012], as the peak frequency of the modulation is entangled with the Gaussian's size. This is to naturally reinforce that smaller Gabor kernels cover higher frequencies (otherwise, the modulation and the envelope can be completely disentangled). We derive the closed-form solution for its analytical Fourier Transform and include detailed steps in the Appendix. Given the peak frequency of the modulation  $f_0 = \|\vec{\omega}\|$ , its final derivation is

$$\mathcal{F}\{g(\mathbf{x})\}(k) = \frac{1}{2} e^{-ik^T \mu} \left[ e^{-\frac{1}{2}(k-f_0)^T \Sigma(k-f_0)} + e^{-\frac{1}{2}(k+f_0)^T \Sigma(k+f_0)} \right] \quad (7)$$

Since we can analytically compute the spectral content of each Gabor kernel, we can easily obtain a good approximation of the band-limited filtered volume by removing the undesired kernels (Figure 2).

### 4.3 Gabor Fields

Inspired by Laplacian and Steerable pyramid decompositions [Simoncelli and Freeman 1995], we pose primitive volumes as the composition of different kernel mixtures, each modelling specific spectral bands. If separated into discrete band-passes or levels, they conform a volumetric Laplacian pyramid, which we can further separate in different orientations to conform a "relaxed" Steerable pyramid (relaxed, as in we do not ensure orthogonality, due to the unlimited theoretical support of Gabor kernels). In practice, we combine positive, zero-frequency Gabor kernels (i.e., Gaussians) for the base of our pyramid (the low-pass), and Gabor kernels ( $f_0 > 0$ ) for the remaining frequencies (residual). Gabor kernels can have both positive and negative density values, which discards them as a valid density function on their own. An example of our "pyramid decomposition" for a regressed asset can be found in Figure 1.

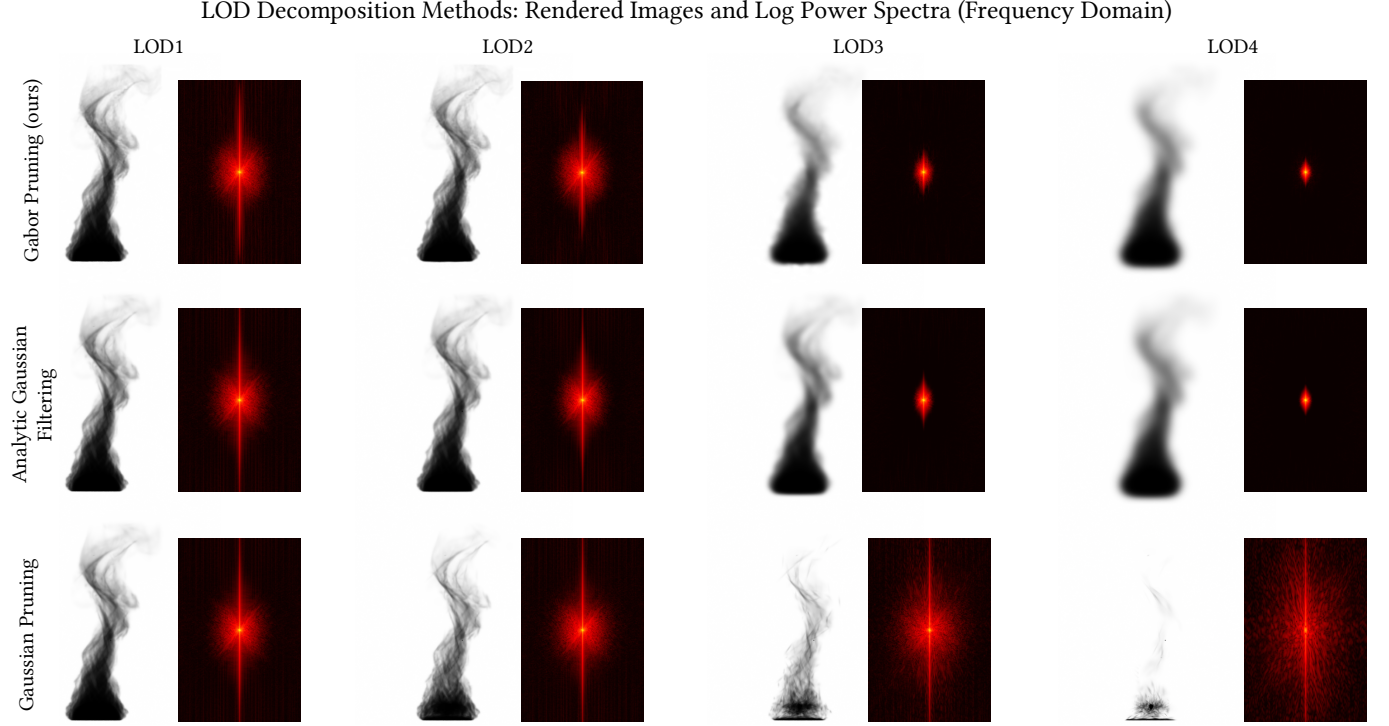


Fig. 2. Comparison of different LOD strategies for primitive-based volumetric representations. In each cell, we show the volume rendering and the corresponding power spectra of the Fourier Transform. Note how, in our method, Gabor Pruning and Gaussian Analytic, the spectra shrink for higher LOD levels. In our case, however, the higher levels consist of a substantially smaller number of primitives, while each level of Gaussian Analytic contains the same number of primitives. A simple Gaussian Pruning fails to create LOD levels with a low-pass characteristic.

While it is easier to think of it as separated "layers", in practice, we have total control over the frequency content, and continuous decompositions are perfectly possible.

#### 4.4 Efficient Physically-based Rendering with Gabor Kernels

A key component in primitive-based volume rendering is the ability to compute transmittance integrals analytically. We thus derive closed-form definite line integrals for the projected 3D anisotropic Gabor kernel along an arbitrary ray. While we include step-by-step derivations in the Appendix, we present here the final integral expressions. For an arbitrary ray  $r = x_0 + \vec{v} \cdot t$ , and transforming the anisotropic Gabor into its canonical (i.e. whitened) local space, the full-domain integral of the projected Gabor kernel  $g_r$  along the ray is

$$\int_{-\infty}^{\infty} g_r(x; \mu, \Sigma, \vec{\omega}) dt = \mathcal{K} e^{-\frac{1}{2}(c-b^2+\Omega^2)} \cos(d - \Omega b) \quad (8)$$

For the segment-definite integral with general bounds  $[t_0, t_1]$ :

$$\int_{t_0}^{t_1} g(r, \omega, \Sigma, \mu) dt = \mathcal{K} e^{-\frac{1}{2}(c-b^2+\Omega^2)} \cos(d - \Omega b) \times \left[ \operatorname{erf}\left(\frac{t_1 + b - i\Omega}{\sqrt{2}}\right) - \operatorname{erf}\left(\frac{t_0 + b - i\Omega}{\sqrt{2}}\right) \right] \quad (9)$$

with

$$b = \mathbf{p}_W \cdot \vec{v}_W, \quad c = \mathbf{p}_W \cdot \mathbf{p}_W$$

$$\Omega = \vec{k}_W \cdot \vec{v}_W, \quad d = \vec{k}_W \cdot \mathbf{p}_W \quad \mathcal{K} = \frac{1}{2\pi\sqrt{|\Sigma| \cdot \|W \cdot \vec{v}\|}} \quad (10)$$

where we define the whitened ray parameters and frequency vector using ZCA whitening matrix  $W$  as:

$$W = R^T S^{-1}, \quad \mathbf{p}_W = W(x_0 - \mu), \quad \vec{v}_W = \frac{W \cdot \vec{v}}{\|W \cdot \vec{v}\|} \quad \vec{k}_W = W \cdot \vec{\omega} \quad (11)$$

Here  $x_0$  and  $\vec{v}$  are the ray origin and direction,  $\mu$  and  $\Sigma$  are the Gabor kernel mean and covariance respectively. The whitened direction  $\vec{w}$  is normalized so that  $\|\vec{v}_W\| = 1$ . The factor  $\|W \cdot \vec{v}\|^{-1}$  is the Jacobian that arises as we normalize  $\vec{v}_W$  to unit length for simpler integration. The integration parameter  $t$  in whitened-normalized space relates

to world space by this factor. The term  $(c - b^2)$  represents the squared perpendicular distance from the kernel center to the ray in canonical space. The complex error function  $\text{erf}(\cdot)$  (Faddeeva function) handles the finite integration bounds.

*Complex-valued Error Function.* A key issue when integrating Gabor kernels analytically is the computation of complex-valued error functions. A number of algorithms can be found in literature [Gautschi 1970; Poppe and Wijers 1990; Zaghoul and Ali 2012], but their accuracy, speed and ability to converge largely depend on the expected range of input arguments. In order to avoid branching on render time among many different algorithms, we implemented a truncated Taylor expansion [Poppe and Wijers 1990] for an effective tradeoff between performance and accuracy, ensuring its convergence for our expected value range. We thus approximate the  $\text{erf}$  term in Equation 9 as:

$$\text{Re}[\text{erf}(z)] \approx \frac{2}{\sqrt{\pi}} \sum_{n=0}^{N-1} \frac{(-1)^n \text{Re}(z^{2n+1})}{n!(2n+1)} \quad (12)$$

With

$$z = \frac{t + b - i\Omega}{\sqrt{2}} \quad (13)$$

*Implementation details.* We implement it in DrJIT with early exits based on the relative size of newer terms in the series with respect to the previous term; in practice, we exploit the symmetries in the pair of  $\text{erf}$  terms to compute them jointly in a single loop. We truncate the series at a maximum of 16 terms to avoid numerical instability and bound the cost of the computation. Since this is a relatively expensive operation, we further optimize performance by catching segment sizes below a manually selected threshold ( $\approx 10^{-4}$  in whitened, local space units) and directly approximating their integral through the midpoint rule. This reduces the computation to a single Gabor probability density function  $\text{pdf}$  evaluation.

*Distance Sampling.* For the inversion of the cumulative density function  $\text{cdf}$  (to enable distance sampling in multiple scattering), we resort to a bisection solver. In practice, most segments overlap with other primitives, requiring the use of solvers for efficiency. Biased alternatives such as uniform sampling along the candidate segment containing a path vertex, can also be employed.

*Adaptive Clamping.* Ray-intersection queries and overlap processing dominate rendering time in volumetric primitive rendering. Reducing the extent (spatial support) of primitives greatly benefits rendering speed; however, reducing below  $3\sigma$  could create artifacts. The specific properties of Gabor kernels allow us to benefit particularly from spatial clamping while keeping error low. We develop a small heuristic to clamp the extent of each of our particles adaptively.

We start from Equation 9. Considering a perpendicular ray (maximum contribution), our goal is to find at which eccentricity from the kernel’s mean the contribution becomes insignificant. While Gabor kernels have infinite zero-crossings due to their harmonic modulation, we can approximate that in the worst-case scenario (with a phase shift producing a cosine term of value 1), their contribution

will be given by the attenuated integral  $\rho$  along the perpendicular ray to  $\vec{\omega}$  at extent  $E = c - b^2$ .

$$\rho(E) = \alpha \cdot \mathcal{K} \cdot \exp\left(-\frac{1}{2}(E^2 + \Omega^2)\right), \quad (14)$$

where  $\alpha$  is the learned opacity scaler (Section 5). Setting  $\rho(E) = \epsilon$  for a threshold  $\epsilon$  (minimum contribution to consider) and solving for the extent:

$$E_{\text{adaptive}} = \sqrt{-2 \ln(2\pi \cdot \epsilon \sqrt{|\Sigma|})} - \vec{k}_W^2, \quad (15)$$

The  $\vec{k}_W^2$  term captures the frequency-induced decay: thus, higher-frequency Gabors can benefit from smaller extents.

For Gaussian primitives ( $f_0 = 0$ ), this simplifies to:

$$E_{\text{adaptive}} = \sqrt{-2 \ln(2\pi \cdot \epsilon \sqrt{|\Sigma|})}, \quad (16)$$

## 4.5 Frequency and Orientation-aware Volume Rendering

Interesting opportunities for acceleration arise when a volume can be decomposed spectrally and angularly. In certain orientations, Gabor kernels have line integral values close to zero. This allows us to simply avoid ray-tracing subsets of the mixture depending on the ray orientation, or importance sample sets of particles based on their frequency, density, and orientation.

In order to explain the concept of orientation selectivity, we plot several Gabor kernels with different frequencies in the spatial domain and their respective power spectrum plots in Fourier space in Figure 3. We also include an animated version of this plot in the Supplementary material. In essence, the projected integral and frequency of a Gabor kernel along a ray is highly dependent on its orientation with respect to the modulation plane. In the extreme case of integrating along the very plane, its integral tends to zero. Higher frequencies (right in Figure 3) exhibit higher orientation selectivity. We further include the integral of an exemplary 3D Gabor kernel along a plane for visualization at different orientations in Figure 4.

*4.5.1 Stochastic Laplacian Path Tracing.* Spectral selectivity enables a number of unorthodox acceleration strategies. Reducing mixture complexity and overlap for a given ray directly delivers substantial improvements in performance. In multiple scattering setups or complex scenes, a substantial amount of variance comes from the recursive nature of the integral itself: while obtaining exact transmittance integrals for every path segment reduces variance, much greater gains may be achieved by simply reducing traversal time across the volume and affording more samples.

Inspired by recent work on stochastic texture filtering [Fajardo et al. 2023] and procedural noise using Monte Carlo sampling [Fajardo and Pharr 2023], we develop a stochastic-analytical estimator: at render time, for each path segment, we stochastically decide which frequency bands of the asset to integrate. This essentially trades off increased variance (or bias, depending on the scenario) per sample with substantially faster traversal time across the volume (as in, reduced intersections in a simpler geometry structure). We propose a number of strategies in the Appendix (Table 5). In particular, we found the control-variate inspired techniques to be a

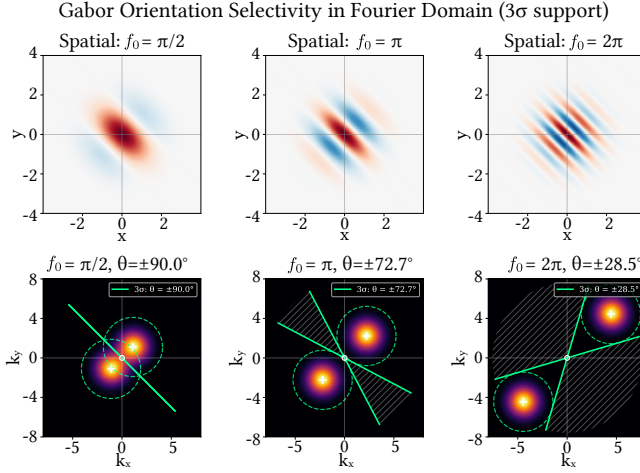


Fig. 3. **Top:** 2D Gabor kernels in the spatial domain with different frequency magnitudes. **Bottom:** their respective power-spectrum representations. Gabor kernels exhibit directional attenuation, effectively modelling residuals in certain frequencies and orientations. As we clip their support to  $3\sigma$ , we can estimate at which orientations, relative to the integrating ray, their contribution decays enough to be considered (shaded area). In our work, we leverage this insight to extract performance by masking non-contributing Gabor kernels before an intersection query is even traced.

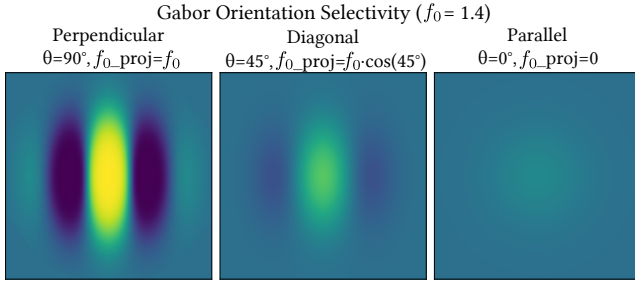


Fig. 4. Visualization of the integral over a plane of a 3D Gabor kernel at different rotations around the Y axis. As we can see, projected frequency and integral magnitude both depend on orientation. In the limit, integrating along its modulation plane causes destructive interference that attenuates the integral value significantly. Higher frequencies see their contributions decay even faster angularly, and to smaller integral magnitudes, as we show in our 2D example in Figure 3.

good compromise between increased rendering performance and variance. This essentially means always including the low-pass (i.e., Gaussian band) within the set of primitives to intersect with, and additionally including another band (or multiple) of higher frequency Gabor kernels. This allows shifting variance or bias to lower or higher frequencies, as desired.

**4.5.2 Stochastic Orientation-selective Path Tracing.** Additionally to sampling from the frequency levels, we can exploit the angular selectivity of the volume to further accelerate rendering.

For a 3D Gabor kernel  $g(x; \mu, \Sigma, \vec{\omega})$  (Equation 6) integrated along a ray with direction  $\vec{v}$ , the contribution depends on the alignment

angle  $\theta$  between  $\vec{v}$  and the frequency direction  $\vec{\omega}$ . Defining  $a = |\cos \theta| \in [0, 1]$  as the alignment factor: when the ray is perpendicular to the frequency direction ( $a = 0$ ), the cosine modulation contributes uniformly along the ray. When parallel ( $a = 1$ ), destructive interference reduces the contribution by  $\mathcal{K} \exp(-f_0^2/2)$ .

We can then implement different strategies to reduce the number of kernels we trace against based on ray direction (Appendix Table 6). In practice, we put the Gabor kernels in a pre-processing step into different bins based on the orientation and frequency of their modulations. During render time, for every new ray, and before we intersect with the scene, we compute its alignment with the representative bin orientations, and based on this alignment and the frequencies contained in the bin, we decide which primitives to mask out and which to include in the set to be "intersected". This choice can be deterministic (i.e. we simply prune low contributing orientations, paying with a small amount of error) or stochastic (i.e. we use importance sampling to sample proportionally from orientations contributing more to the given ray). For importance sampling, the sampling weight is essentially the damped contribution by the projected frequency along the ray:

$$w(a) = e^{-\frac{f_0^2 a^2}{2}} \quad (17)$$

We showcase this in a Supplementary material video (rotating BUNNY). Both directional and Laplacian strategies can be used jointly, incrementing the performance boost.

**4.5.3 Analysis on Bias.** For individual segments, both proposed methods are unbiased. A renderer computing just ray transmittance integrals or tomographic reconstruction would be unbiased. However, this is not the case in multiple scattering settings, due to Jensen's inequality. Let  $f$  be a convex function (in our case, an exponential) and  $X$  a random variable. Jensen's inequality states:

$$f(\mathbb{E}[X]) \leq \mathbb{E}[f(X)]. \quad (18)$$

resulting in a biased estimator of transmittance, despite our density integral estimator being unbiased.

We can quantify the bias using a second-order Taylor expansion of  $e^{-\hat{\tau}}$  around  $\mathbb{E}[\hat{\tau}]$ :

$$\mathbb{E}[e^{-\hat{\tau}}] \approx e^{-\mathbb{E}[\hat{\tau}]} + \frac{1}{2} \text{Var}(\hat{\tau}) \cdot e^{-\mathbb{E}[\hat{\tau}]} \quad (19)$$

Therefore:

$$\text{Bias} = \mathbb{E}[\hat{T}] - T_{\text{true}} \approx \frac{1}{2} \text{Var}(\hat{\tau}) \cdot T_{\text{true}} > 0 \quad (20)$$

The bias is thus proportional to the variance of the optical depth estimator and the true transmittance (smaller  $\tau$  means larger relative bias). Tuning the sampling strategy for specific needs and assets can reduce such bias (i.e. importance sampling based on the total energy of a pyramid level), or steer it in a perceptually-kind manner (by shifting error to specific spatial frequencies).

#### 4.6 Implementation Details

We implement our method in Mitsuba 3 [Jakob et al. 2022], using a modified version of VPPT [Condor et al. 2025]. To maximize performance, we partition the assets at load time into a pyramid of frequencies and orientations, in order to leverage Optix ray visibility masking at the Top-level Acceleration Structure (TLAS). We extended Mitsuba 3 to support ray visibility masking, such that we can selectively decide which levels of the pyramid to integrate/interact with before even traversing the BVH. In practice, this means that each level has its own Geometry Acceleration Structure (GAS), which may be suboptimal but turns out to be more efficient than rejecting primitives after the intersection routine.

More concretely, each pyramid level  $l$  is assigned a visibility mask:

$$\mathcal{V}_l = 2^l \quad (21)$$

The ray carries a mask  $\mathcal{V}_r$  whose active bits are sampled according to some strategy (see Table 6). We compute a bit-wise AND between ray and visibility masks during intersection tests. Only primitives with common active bits (e.g.,  $(\mathcal{V}_r \wedge \mathcal{V}_l) \neq 0$ ) are considered.

As an example, for a single ray, the rendering pipeline proceeds as follows:

- (1) Sample a pyramid level based on the chosen strategy.
- (2) Set the bits in  $\mathcal{V}_r$  according to the sampling outcome.
- (3) Perform ray-primitive intersection (filtered by mask) collecting overlapping primitives along the ray.
- (4) Distance sampling (multiple-scattering, VPPT) OR integrate the projected field directly (tomography).
- (5) Reweight integrals based on sampling probabilities.
- (6) Recurse ray (multiple scattering).

In the tomography case, only after all samples are collected, we turn accumulated density into a transmittance estimate, assuming exponentially decaying media, as  $T = \exp(-\tau)$ ; this makes it an unbiased estimator. While collecting the product of individual transmittances is mathematically equivalent, our density importance sampling strategy would make it a biased estimator (see Jensen’s inequality above).

In practice, primary path and secondary rays (i.e. next-event estimation, NEE) can also use different strategies: for NEE in particular, we can heavily skew the sampling towards the Gaussian level of the pyramid, which contains most of the energy in the volume, drastically reducing rendering time. We explore some of these in Section 6 as well.

### 5 Regressing Gabor Fields

In order to transform discrete density fields (voxel grids) into Gabor Fields, we develop a novel regression scheme specifically tailored to our method.

#### 5.1 Hierarchical Differentiable Rendering-Based Kernel Regression

Similarly to stochastic sliced Wasserstein regression [Kolouri et al. 2019], Condor et al [2025] proposed a regression scheme based on image-based differentiable rendering, optionally warm-started on a Gaussian mixture obtained through expectation-maximization.

While their approach is effective with simple and low-resolution assets, it does not scale well. This can be inferred by the limited complexity shown on high-resolution assets such as the Walt Disney Cloud<sup>1</sup>. We attribute this to 1) the limited representation or modeling power of individual Gaussians and 2) scalability issues of an end-to-end regression scheme. Our proposed Gabor kernels improves on 1), and we leverage the strengths of these kernels by coupling them with a hierarchical regression procedure with tight controls over the frequencies modeled during regression.

*Volume Filtering.* We create a Gaussian pyramid  $G_l$  with a spatial standard deviation  $\sigma_l$  that has the same perceived blur irrespective of grid resolution. Doing so simplifies the optimization of the lowest level, as the frequency range is fixed for all voxel grids. To achieve this, we work in a normalized continuous domain  $\Omega = [0, 1]^3$ . At level  $l$ , we define  $\sigma_l = \sigma_0 2^l$ , where  $\sigma_0$  (in normalized units) controls the blur radius at the finest scale. A larger  $\sigma_0$  corresponds to stronger blur at all levels. For a discrete voxel grid of resolution,  $N_x \times N_y \times N_z$ , let  $N_{\max} = \max(N_x, N_y, N_z)$ . We map normalized coordinates to voxel indices by  $x = uN_{\max}$ ,  $u \in \Omega$ . The corresponding standard deviation in voxel units is

$$\sigma_l^{\text{vox}} = \sigma_l N_{\max}. \quad (22)$$

*Hierarchical Regression.* To distill voxel density grids into a hierarchical Gabor field, we first build the Gaussian pyramid  $\{G_l\}_{l=0,\dots,K}$  using eq. (22) with  $\sigma_0 = \frac{1}{120\pi}$ . The lowest level (typically 3 or 4) contains the lowest frequencies. All voxel grids are zero-padded to match  $N_{\max}$  in all dimensions and placed in a  $[-1, 1]^3$  cube to render reference images. We render tomographic reference images using ratio tracking [Novák et al. 2014] with a high count of samples per pixel. We sample cameras from a hemisphere surrounding the  $[-1, 1]^3$  cube. We directly fit a Gaussian mixture to the lowest level. The remaining levels are jointly fit by a single Gabor mixture.

*Initialization.* We derive analytic formulas to define the exact frequency band that our mixture has to model. The Gaussian kernels model the lowest frequency band, and their scale solely determines their spectral footprint. The smallest appropriate scale for each level  $l$  is given by

$$s_{\min}(l) = L\sigma_0 2^l, \quad (23)$$

where  $L$  is the size of the continuous domain. The Nyquist scale depends on the grid’s resolution and is given by

$$s^{\text{NY}} = \frac{L\sqrt{2\log\frac{1}{\epsilon}}}{\pi N_{\max}}, \quad (24)$$

where  $\epsilon$  is the effective cutoff, e.g., the magnitude response of the Gaussian filter at the cutoff frequency  $|H(f_c)| = \epsilon$ . We choose  $\epsilon = 0.25$ . We sample the scales for the base layer using  $s_{\text{high}} = s_{\min}(l_{\text{base}} + 1)$  and  $s_{\text{low}} = s_{\min}(l_{\text{base}})$  by drawing from a Normal distribution:

$$s_{\text{init}} \sim \left| \mathcal{N} \left( 0, \frac{s_{\text{high}} - s_{\text{low}}}{3} \right) \right| + s_{\text{low}}. \quad (25)$$

For the Gabor kernels, we use  $s_{\text{low}} = 1.5 s^{\text{NY}} \omega_{\text{high}}$  instead, thereby biasing the initialization to higher frequencies. We initialize the rotations randomly and  $\omega_{\text{init}} \sim \text{Unif}[0.7, 1.5]$ . Centers are sampled from

<sup>1</sup><https://disneyanimation.com/data-sets/>

non-empty voxel locations to ensure good coverage, and opacities are drawn from  $\alpha_{\text{init}} \mathcal{N}(1, \frac{1}{4})$  where  $\alpha_{\text{init}}$  is the only hyperparameter adjusted depending on the reference voxel grid's density.

*Optimization Procedure.* We follow the image-based differentiable rendering regression scheme introduced by Condor et al. Since Gabor kernels are not valid probability distributions, we can not warm start using expectation-maximization. Inspired by Kheradmand et al., we define our optimization procedure as a stochastic sampling process from the underlying density distribution. This enables stronger exploration during early optimization and defines strategies to relocate unused primitives throughout the optimization. They show that optimization steps can be converted to Stochastic Gradient Langevin Dynamics by injecting noise into the gradients. The gradient update for a single Gaussian or Gabor kernel  $\mathbf{g}$  becomes

$$\mathbf{g} \leftarrow \mathbf{g} - \lambda_{\text{lr}} \cdot \nabla_{\mathbf{g}} \mathbb{E}_{\mathbf{I} \sim \mathcal{I}} [\mathcal{L}(\mathbf{g}; \mathbf{I})] + \lambda_{\text{noise}} \cdot \epsilon, \quad (26)$$

where  $\epsilon$  is the gradient noise facilitating exploration,  $\lambda_{\text{noise}}$  controls the noise magnitude,  $\lambda_{\text{lr}}$  is the learning rate, and  $\mathbf{I}$  is an image sampled from the training dataset  $\mathcal{I}$ . In practice, we compute the gradients over 32 renderings and use the Adam [Kingma and Ba 2014] optimizer update for  $\nabla_{\mathbf{g}} \mathbb{E}_{\mathbf{I} \sim \mathcal{I}} [\mathcal{L}(\mathbf{g}; \mathbf{I})]$ . We follow Kheradmand et al. [2024] and only add gradient noise for the centers  $\mu$ . The noise term is given by

$$\epsilon_{\mu} = \lambda_{\text{lr}} \cdot \text{sigmoid}(-100(t - \alpha)) \cdot \Sigma \eta, \quad \eta \sim \mathcal{N}(0, 1), \quad (27)$$

where  $\alpha, \Sigma$  is the primitive's weight and covariance,  $t$  is a hyperparameter and set to  $1e - 6$ , which we later use as a threshold to determine primitives to be resampled. The sigmoid term reduces noise around the threshold to ensure a smooth decay for subsequent resampling. Essentially, we inject anisotropic noise identical to the primitive's Gaussian envelope.

*Resampling Primitives.* For a stable optimization, it is crucial to ensure that the resampled primitives blend well into the current asset. The underlying idea is to teleport "dead" primitives (weight  $\alpha_i < 1e - 6$ ) to alive primitives and update their parameters to minimize visual change. The parameter update of Kheradmand et al. was developed for rasterization; therefore we re-derive it for analytic ray tracing. All dead primitives will be teleported to a live primitive which we sample with probabilities proportional to their integral. The 3D integral of a Gabor kernel is given by

$$\int g(x; \mu, \Sigma, \omega) = \frac{\alpha}{(2\pi)^{\frac{3}{2}} |\Sigma|^{\frac{1}{2}} e^{-\frac{3}{2}\omega^2}}. \quad (28)$$

Consider primitives  $g_{1, \dots, N-1}$  being teleported to the alive primitive  $g_N$ . The new parameters are given by:

$$\begin{aligned} \mu_{1, \dots, N}^{\text{new}} &= \mu_N^{\text{old}}, & \alpha_{1, \dots, N}^{\text{new}} &= \frac{\alpha_N^{\text{old}}}{N} \\ \Sigma_{1, \dots, N}^{\text{new}} &= \Sigma_N^{\text{old}}, & \omega_{1, \dots, N}^{\text{new}} &= \omega_N^{\text{old}}, \end{aligned} \quad (29)$$

This update keeps the density field of the mixture almost constant, except for the negligible loss of density at the location of the previously "dead" primitives. To further facilitate exploration, we keep the momentum statistics of Adam for the revived primitives but reset them for the sampled live primitives to discourage big movements.

*Loss Definition.* The main component of our loss is a mix of SSIM [Wang et al. 2004] and L1. We further add regularization terms to favor smaller scales to improve render times and a weight decay facilitating compact assets such that unused primitives can be resampled or later pruned. Opposed to Gaussian kernels, constraining the frequency content of anisotropic Gabor kernels is substantially more difficult, as limiting a single parameter like the scale will not suffice. As seen in Figure 3, depending on their orientation and peak frequency of their harmonic modulation  $\omega$ , their spectral footprint changes drastically. To avoid aliasing, we derive a regularization term as a soft constraint. The angular cutoff frequency of each layer is given by

$$\phi^{\text{cutoff}}(l) = \frac{\sqrt{2 \log \frac{1}{\epsilon}}}{\sigma_0 L 2^l}, \quad (30)$$

and the angular Nyquist frequency yields the upper bound.

$$\phi^{\text{NY}} = \frac{\pi N_{\text{max}}}{L} \quad (31)$$

We propose

$$\mathcal{L}_{\text{freq}} = \sum_i \text{sigmoid} \left( a(f_{0,i} - \phi^{\text{NY}}) \right), \quad (32)$$

where  $a = 10$  is a hyperparameter creating a steep transition, effectively activating the regularization term only when the peak frequency comes close to aliasing. The final loss term is given by

$$\begin{aligned} \mathcal{L} &= 0.80 \cdot \mathcal{L}_{\text{L1}} + 0.20 \cdot \mathcal{L}_{\text{SSIM}} + \mathcal{L}_{\text{freq}} \\ &+ \lambda_{\alpha} \cdot \sum_i |\alpha_i| + \lambda_s \cdot \sum_i |s_i|_1 \end{aligned} \quad (33)$$

*Implementation Details.* We optimize our mixture models for 300 iterations using a cosine learning rate scheduler. We resample "dead" primitives every 30 iterations and have an exponential decay on the gradient noise level  $\lambda_{\text{noise}}^{\text{it}} = \lambda_{\text{noise}}^0 \cdot \gamma^{\text{it}}$ , where  $\gamma = 0.65$ . We include our final hyperparameters in the Appendix (Table 7). We further ablated the influence of our components in an Ablation study in Table 2. Optimizing the low frequency layer usually takes 2-8 minutes and the full volume between 0.1-2h (RTX 4090) depending on asset size and the number of primitives.

## 6 Results

In this section, we compare our proposed modeling approach in terms of storage, regression quality, and rendering speed against previous works on classic voxel grid distributions and Gaussian primitive volumes [Condor et al. 2025]. We also showcase novel rendering approaches that exploit the orientation- and frequency-selectivity of our decomposition to improve rendering performance and enable new applications. Unless stated differently, we use 32 views at approx. 768×768 px resolution to optimize the assets.

### 6.1 Regression Quality and Compression

In Table 3, we compare Gabor Fields against Gaussian Primitive volumes [Condor et al. 2025], regressed with our own pipeline for a fair comparison, as the code for the full optimization process has not been released by the authors. We also include compression details in Table 4, against compressed voxel grids, as well as Gaussian volumes. For the same number of primitives, Gaussian kernels are slightly

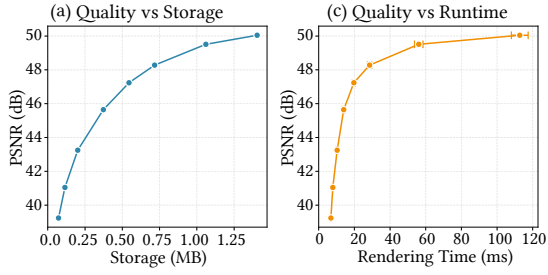


Fig. 5. Scalability evaluation of Gabor-based representations on the TORNADO dataset. The primitive count ranged from 1,024 to 32,768, with an additional 768 base Gaussian primitives. PSNR was measured with respect to the original voxel grid, and runtime was averaged over 50 runs. Storage costs assume 32-bit floating-point precision without compression. Measured on an RTX 4090.

Table 2. Ablation study on the BUNNY volume with  $300 \times 300$  resolution. PSNR  $\Delta$  shown relative to the full method. Runtime was averaged over 50 runs on an RTX 4090.

Ablation	PSNR $\uparrow$ (dB)	$\Delta$ $\uparrow$ (dB)	SSIM $\uparrow$	LPIPS $\downarrow$	Render $\downarrow$ (ms)
<b>Full Method</b>	<b>48.86</b>	<b>+0.00</b>	<b>0.9996</b>	<b>0.0073</b>	<b>24.1</b>
w/o Scale Regu.	48.78	-0.08	0.9996	0.0089	37.7
w/o Trainable $\omega$	48.66	-0.20	0.9995	0.0078	27.3
w/o Frequency Regu.	46.95	-1.92	0.9994	0.0102	26.9
w/o Importance Sampling Centers	46.36	-2.50	0.9993	0.0170	38.0
w/o Opacity Regu.	45.50	-3.37	0.9991	0.0133	31.0

more compact, as we include an extra parameter per particle ( $\omega$ ). However, we also achieve superior quality, which becomes evident in the higher quality of details in Figure 9 where we showcase a variety of different assets. In Figure 5 we study how quality scales with the number of primitives for both Gabor and Gaussian assets. Further, we fit all individual frames of the animated TORNADO asset<sup>2</sup>, without hand-tuning of optimization parameters for individual volumes, to demonstrate the robustness and quality of our optimization. A rendered animation of the TORNADO asset is available in the Supplementary material. Additionally, we include an ablation to validate our choices in our regression method in Table 2. In general, Gabor Fields retain the compactness and quality of Gaussian Primitive Volumes, while providing fine-grained spectral control and a myriad of acceleration opportunities.

## 6.2 Rendering Performance

**6.2.1 Stochastic Laplacian and Orientation-selective rendering.** We showcase several configurations for stochastic Laplacian rendering in Figure 7. We include an analysis on previously reported strategies in Figure 6. We also include a video showcasing orientation-selective strategies in the Supplementary material. While analytic rendering provides the best quality vs time tradeoff, stochastic methods can

<sup>2</sup><https://jangafx.com/software/embergen/download/free-vdb-animations>

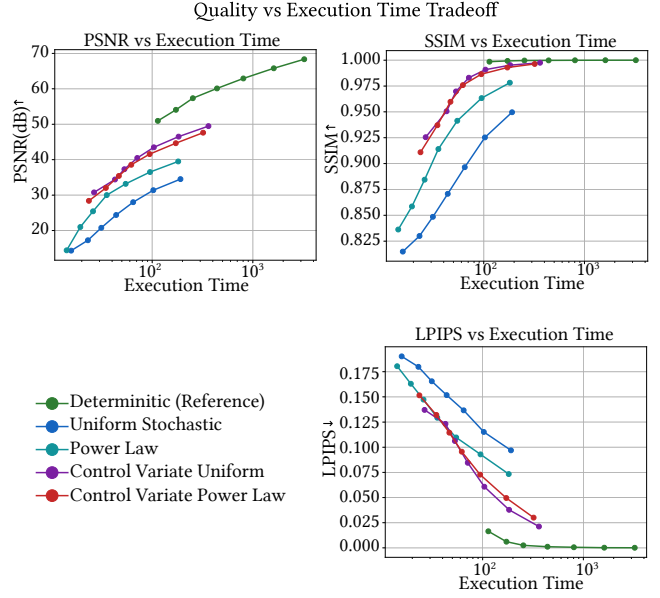


Fig. 6. Quality vs rendering time with the different stochastic-analytical estimators (see Appendix Table 5). Starting from 1spp, each dot represents powers-of-two extra samples per pixel (1,2,4,8,etc).

Reference      Uniform Sampling (1spp)      Control Variate Power Law (1spp)

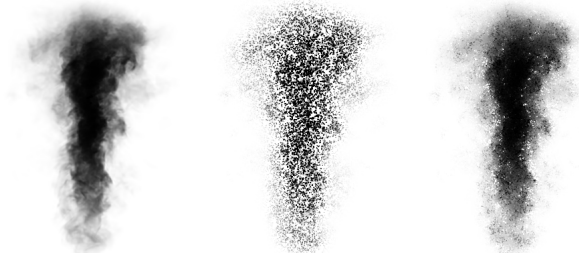


Fig. 7. Some renders with our stochastic-analytical rendering methods (TORNADO).

reduce significantly per-sample cost, which may be interesting in some applications. In tomographic rendering, these methods are unbiased.

We also run an ablation with the TORNADO dataset trained with 33k particles on the choice of our parameter  $\beta$  for the *control variate power law* setup in Figure 8. Substantial acceleration is possible for some increased variance.

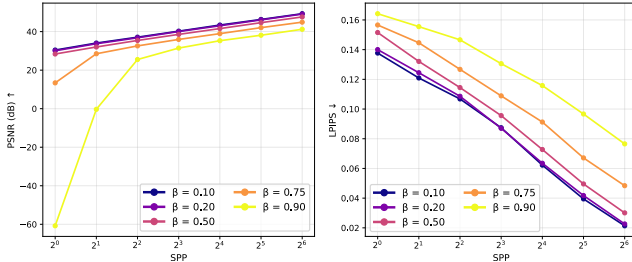
**6.2.2 Path Tracing with Multiple Scattering.** We compare rendering performance and quality against Gaussian Primitive Volumes [Condor et al. 2025] in Figure 9. Additional examples of higher quality renders with our Gabor Field Path Tracer can be seen in Figures 1, 10 and 11. For a fair comparison, we allow Gaussian volumes to benefit from the same acceleration strategies we describe for Gabor Fields in

Table 3. Comparison of Gabor and Gaussian kernel performance on volumetric assets tomography regression. We report WDAS CLOUD at  $\frac{1}{8}$  resolution.

Asset	PSNR ↑		SSIM ↑		L1 ↓		L2 ↓		LPIPS ↓		#Primitives ↓	
	Gabor	Gauss	Gabor	Gauss	Gabor	Gauss	Gabor	Gauss	Gabor	Gauss	Gabor	Gauss
DUST DEVIL	<b>52.54</b>	49.12	<b>0.9997</b>	0.9987	<b>0.000868</b>	0.001382	<b>0.000006</b>	0.000012	<b>0.0068</b>	0.0161	24,576	24,576
EXPLOSION	<b>53.12</b>	51.47	<b>0.9998</b>	0.9997	<b>0.001072</b>	0.001335	<b>0.000005</b>	0.000007	<b>0.0030</b>	0.0067	24,576	24,576
FIRE	<b>51.13</b>	49.22	<b>0.9996</b>	0.9988	<b>0.001218</b>	0.001692	<b>0.000008</b>	0.000012	<b>0.0145</b>	0.0226	24,576	24,576
SMOKE	<b>50.08</b>	47.20	<b>0.9996</b>	0.9982	<b>0.001190</b>	0.001999	<b>0.000010</b>	0.000019	<b>0.0087</b>	0.0187	16,384	16,384
WDAS CLOUD	<b>47.15</b>	46.92	0.9987	<b>0.9988</b>	0.002045	<b>0.002044</b>	<b>0.000019</b>	0.000020	0.0424	<b>0.0416</b>	24,576	24,576
<b>Average</b>	<b>50.80</b>	48.79	<b>0.9995</b>	0.9988	<b>0.001278</b>	0.001690	<b>0.000009</b>	0.000014	<b>0.0151</b>	0.0211	22,937	22,937

Table 4. Memory footprint analysis for Gabor and Gaussian mixtures with an equal amount of primitives, optimized for maximum quality vs. memory footprint of a voxel grid, compressed to include only non-empty voxels. We report WDAS CLOUD at  $\frac{1}{8}$  resolution.

Asset	Voxels	#Prim	Gabor (MB)	Gauss (MB)	Voxel Grid (MB)
BUNNY	144M	32,768	1.38	0.94	578.24
TORNADO	78M	24,576	1.03	0.94	314.90
DUST DEVIL	18.7M	24,576	1.03	0.94	71.16
EXPLOSION	12.6M	24,576	1.03	0.94	47.97
FIRE	9.0M	24,576	1.03	0.94	34.20
SMOKE	2.8M	16,384	0.69	0.62	10.53
WDAS CLOUD	13.0M	24,576	1.03	0.94	49.77

Fig. 8. We ablate the choice of curve shape  $\beta$  in our Control Variate Power Law strategy, for tomographic reconstruction in the TORNADO asset.

Section 4.6: small-segment integral approximation, adaptive clamping and whitened-space integration. Still, our Gabor Fields routinely outperform Gaussian Primitive Volumes in performance at roughly equal variance. This is still without any frequency or angular-based acceleration technique, rendering at the highest possible detail. On top of improved performance, we can observe higher quality detail, particularly in the higher frequency content (e.g. smoke plume on the first row); this is in line with the superior regression results we report in Table 3. At the same time, if LOD is required, our method will also outperform Gaussian volumes in terms of memory, as it can be naturally filtered rightaway, while Gaussian Primitives would need additional storage for e.g. a volumetric mipmap (Figure 2).

*Biased Acceleration strategies.* The amount of bias with spectral and orientation-selective acceleration techniques depends largely on the scene and strategy selected; we do a short showcase for

an example scene in Figure 10. As can be observed, substantial performance can be extracted for a small exactness or quality price, with full control over the spectral content of the error.

### 6.3 Level of Detail

A prime application of our method is providing seamless LOD. We showcase it in Figures 1, 11 and 2 and in the Supplementary materials, where we include videos of cameras zooming in and out of one of our assets, and a static visualization for comparison. In particular, in Figure 2, we compare it against two baseline approaches for providing LoD in Gaussian-based volumes: analytical filtering of the Gaussians, and pruning-based bandlimiting. While the former provides perfect filtering, it does so at a substantial performance and memory cost. In the second approach, since Gaussians modelling high frequencies also model low frequencies (their power spectrum’s mean is located at 0), pruning high frequency Gaussians results in degraded quality. This can be seen more prominently in the Fourier power spectra of the three examples.

In contrast, our work seamlessly supports LoD rendering; for any given desired frequency limit, we can select the minimal asset that matches the criteria, by simply masking out part of the Gabor kernels.

## 7 Other Applications

Our representation can be useful in other applications where frequency and/or orientation selectivity is critical. Here we demonstrate applications to foveated rendering, motion blur and procedural asset generation.

### 7.1 Foveated Rendering

Similar to LOD control, our Gabor-based representation can be used for foveated rendering to reduce rendering costs when the observer’s gaze location is provided [Guenter et al. 2012; Mohanto et al. 2022; Surace et al. 2023]. A common approach is to reduce the rendering resolution in peripheral vision, which can be easily achieved by progressively discarding Gabor primitives as the distance from the gaze location (i.e., eccentricity) increases. This can be done on a per-ray basis at render time.

We have implemented foveated rendering by assuming a linear relationship between eccentricity and the frequency threshold for discarding primitives. While correct foveation should consider the limitations of the human visual system [Strasburger et al. 2011], we focus here on demonstrating a proof-of-concept implementation.

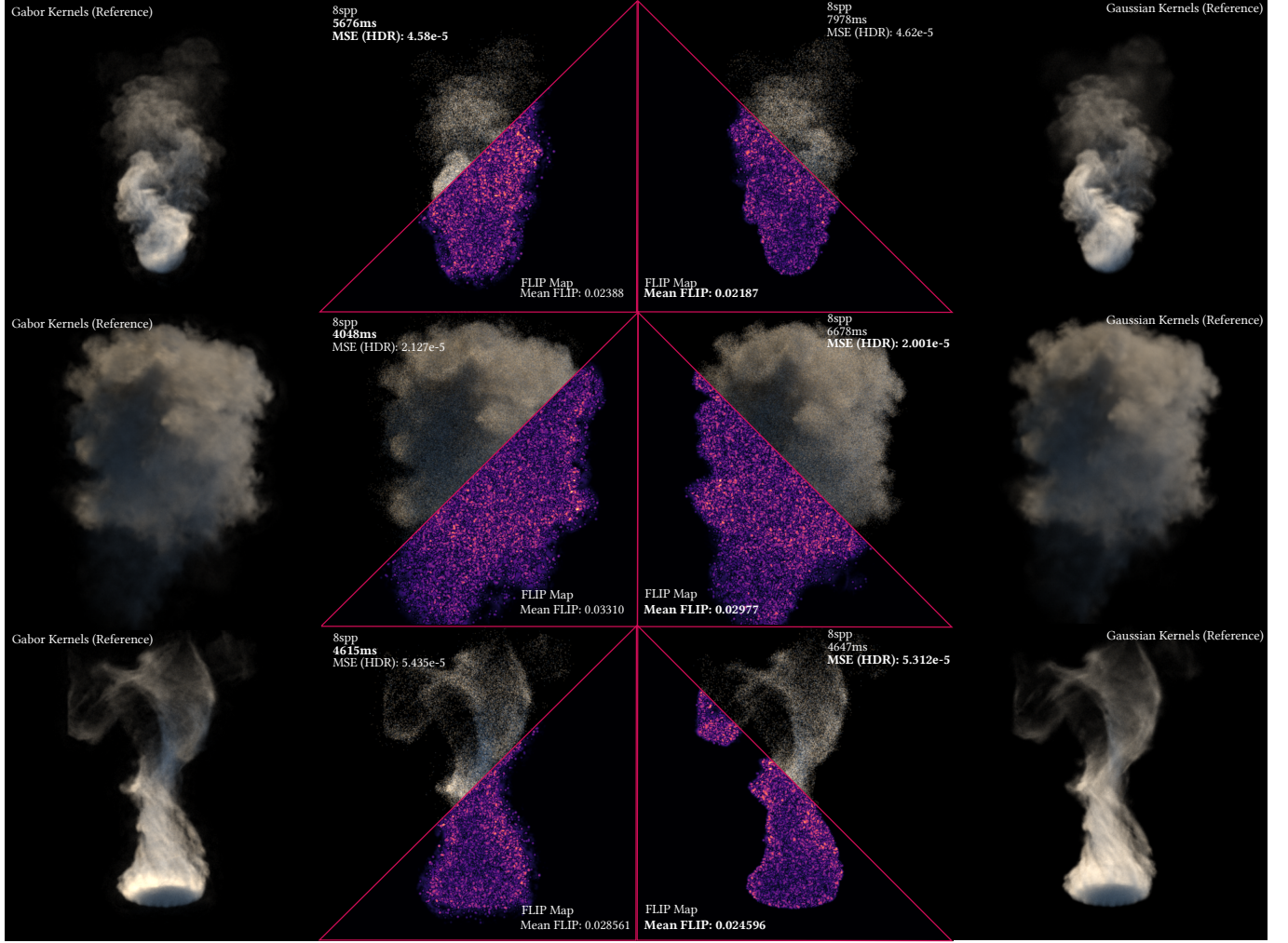


Fig. 9. Comparison of Gabor Fields (Ours) vs Gaussian Primitive Volumes [Condor et al. 2025], for the assets, from top to bottom: SMOKE, EXPLOSION and DUST DEVIL. For roughly equal variance, and primitive count, Gabor Fields are not only faster, but higher quality, featuring higher frequency detail, as reported in Table 3. Times reported measured on an RTX 4090.

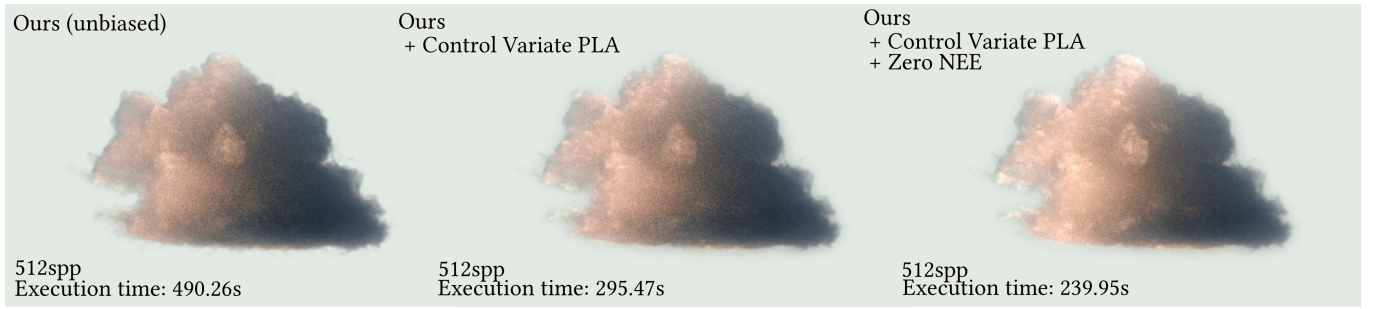


Fig. 10. Showcase of different acceleration strategies enabled by our method with a DISNEY CLOUD dataset with 24k Gabor Kernels. Control Variate Power Law Accumulating (see supplementary Table 5) is used on primary paths, biasing slightly at high frequencies, given our choice of  $\beta = 0.2$ . Zero NEE indicates that for secondary paths (next-event estimation), we only trace against the Gaussian level. This is a powerful strategy, as most of the energy in the density field is contained in the Gaussian level, with Gabors only modelling residual densities. This yields a substantial performance gain (up to 2x in this example) in exchange for some amount of error, which may be acceptable in some situations. Timings reported on an RTX 4090.

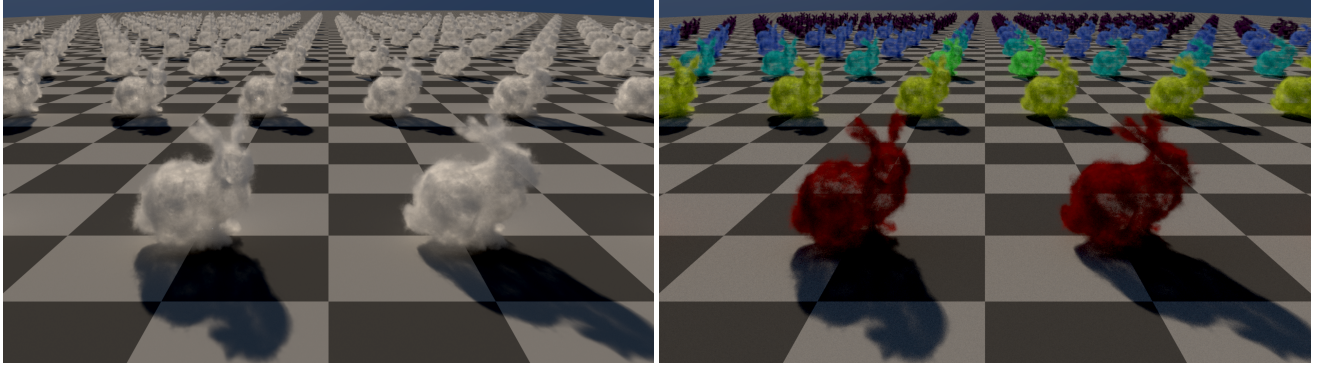


Fig. 11. Stress-test of our LOD strategy using multiple-scattering. Each BUNNY is composed of 33,280 Gabor kernels. We place 176 of them, which amounts to 5,857,280 primitives. Using our Laplacian decomposition we can directly filter them on demand during render time, significantly accelerating rendering speed and eliminating aliasing. In the end, this frame featured an effective count of 759,164 primitives (x7.7 smaller). We visualize the chosen LOD levels on the right with colorized albedos.

For each pixel, we first discard all levels that contain Gabor primitives with frequencies above the threshold. This step provides the most significant efficiency boost, as we can mask entire hierarchy levels, significantly reducing the cost of BVH traversal. Since the levels are discrete, this strategy does not provide truly continuous foveation. To improve continuity, we can check each remaining primitive’s frequency content for the given ray direction and prevent its integration if its frequency falls below the threshold. The checks and additional code branching, however, make it slightly slower than pure level masking, although it depends on the asset and frequency distributions within each level. As the final step, we apply stochastic smoothing by randomly perturbing the per-pixel frequency threshold around transitions between levels.

Figure 12 demonstrates an example of applying the above strategy. Our method reduces both the primitive count via level masking and the integration cost by discarding individual primitives, continuous masking. The primary bottleneck is still BVH traversal. Our approach can be further combined with stochastic and directional rendering strategies (Section 4.5) to reduce sample cost at the periphery. Furthermore, higher acceleration can be achieved with adaptive resolution. In our demonstration, we focus only on truncating the representation. Finally, given that real-time ray tracing suffers from limited sample budgets, combining tight control over spectral content with post-rendering filtering techniques, such as [Edelsten et al. 2019], can yield better results. For example, accounting for denoising capabilities could enable more aggressive removal of the Gabor primitives [Karpenko et al. 2025].

## 7.2 Motion Blur

Our representation provides an efficient way to filter primitives for motion-blur rendering. In particular, it can be used to discard primitives that contribute little to the motion-blur image at an early stage due to their frequency or orientation. One specific example is when a Gabor primitive moves half a cycle in the wave-plane direction, and the pair of original and shifted primitives cancel each other. This observation can be leveraged to reduce the cost of synthesizing

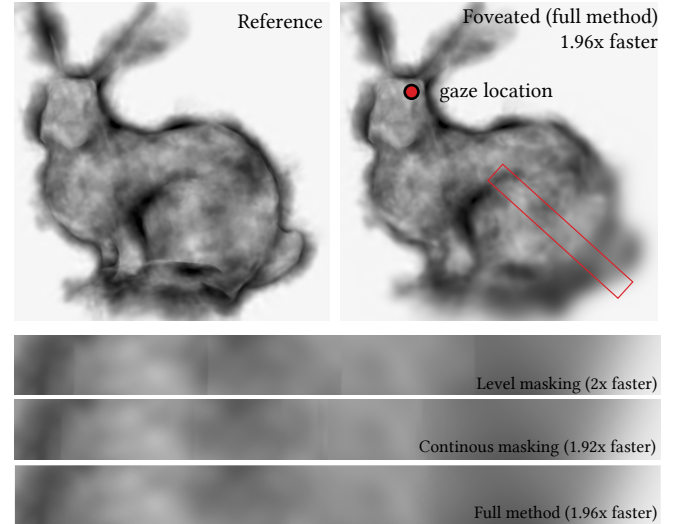


Fig. 12. Results of proof-of-concept foveated rendering. The figure shows the full reference on the left and our foveated version on the right. The insets present different versions of our method with overall speedup with respect to the reference rendering. Note that under realistic foveated rendering conditions (i.e. following the CSF and proper eccentricity decay) level transitions in Level masking mode would be invisible.

motion blur, either by tuning sampling weights for specific directions and frequencies (Section 4.4) or by not considering primitives that contribute little to the final image.

In our simple motion blur implementation, we assume objects to move along the direction  $\vec{d}$  with motion magnitude  $m$ . We model motion blur as a convolution with a 1D box filter oriented in direction  $\vec{d}$  and with size  $m$ . In the frequency domain, this filter has a sinc function profile that attenuates frequencies aligned with the motion direction. For a Gabor kernel with modulation  $\vec{\omega}$  this attenuation can be derived as:



Fig. 13. Results of our proof-of-concept efficient motion blur implementation using the WDAS CLOUD. We compute the expected attenuation for a given linear motion (direction and magnitude), given an orientation and frequency decomposition of an asset (in this case, 3 frequencies and 3 orientations). At the start of rendering, we define ray visibility masks given this attenuation and a manually selected threshold, which results in culling two orientations at two frequency levels, amounting to a 23% reduction in the number of particles. This renders a substantial performance uplift at minimal error, validating our attenuation model.

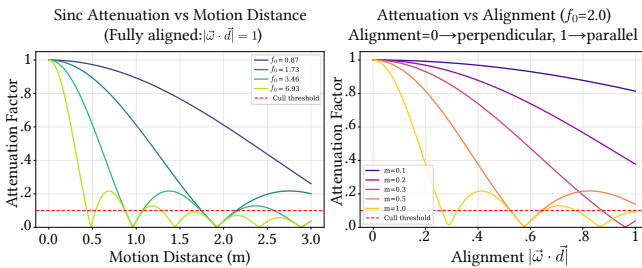


Fig. 14. Behaviour of motion blur attenuation for different motion magnitudes, directions, and Gabor frequencies, and an arbitrary cutoff threshold.

$$\text{attenuation} = \left| \text{sinc}(m |\vec{\omega} \cdot \vec{d}|) \right| \quad (34)$$

The alignment of  $\vec{\omega}$  and  $\vec{d}$  directly influences the attenuation. As the vectors get more parallel to each other,  $|\vec{\omega} \cdot \vec{d}|$  approaches  $f_0 = \|\vec{\omega}\|$ , the motion causes destructive interference, especially for small Gabor primitives. Conversely, when the vectors become perpendicular, the primitives are not attenuated and fully contribute to the resulting image. Note that this analysis holds for any motion in 3D regardless of the camera orientation. We present the analysis of the attenuation function in Figure 14.

To implement this strategy, we first group Gabor primitives into bins  $B_i$  containing different orientations and frequencies. Given motion parameters  $(\vec{d}, m)$ , we cull bin  $i$ , if the attenuation for the mean frequency and orientation in that bin falls below a fixed threshold.

Figure 13 shows an example of applying our technique to an asset decomposed into 3 frequencies, 3 orientation bins, and 1 base Gaussian. For linear motion closely aligned with one of these bins, and  $m = 0.5$ , we achieve a speedup of 1.78x over rendering the full asset, while obtaining almost the same result. This result is despite our Gabor kernels having low  $f_0$ , which reduces their orientation selectivity, and a sparse set of bins covering a large range of orientations and frequencies, pointing to the practicality of the approach. Adapting directional importance sampling techniques could yield

further efficiency gains and quality-speed trade-offs, as many combinations of motion directions and magnitudes result in significant attenuation. We consider this as an interesting extension.

### 7.3 Procedural Cloud Authoring Tool

Inspired by the gradient noise density erosion common in industry [Fajardo and Pharr 2023; Wrenninge et al. 2011], we created our own authoring pipeline for cloud generation that leverages our volume representation. Through an interactive application, users can generate clouds that can be rendered directly with our approach without the need for any regression. To create a realistic cloud, we start by defining a cloud chunk similar to textured ellipsoids [Gardner 1985]. A cloud chunk is defined using a Gaussian kernel and several Gabor kernels on its surface. This way, we can represent the core of a cloud and the splittings and wispy look caused by effects such as wind. For the placement of Gabor kernels, we first define a grid on the surface. Similar to Gabor noise, a Gabor kernel is generated within a random position inside each grid cell [Galerne et al. 2012; Lagae et al. 2009]. The frequency and the orientation of these Gabor kernels are randomly picked from a uniform distribution. Scales of the kernels, on the other hand, are randomized using a Maxwell distribution [Wu and McFarquhar 2018], which provides a physical intuition for the stability of the cloud.

Even though our cloud chunk can model the microstructure of a cloud, a typical cloud consists of several levels. A cloud can form a smaller cloud on its surface when inner pressure builds. To model this behavior, inspired by Bouthors and Neyret [2004] and Dobashi et al. [2000], we define our cloud structure as a tree of cloud chunks. Generated like a fractal, multi-layer clouds have smaller cloud chunks at their surfaces. These smaller chunks are placed uniformly at random on the surface, with the radius drawn from a Maxwell distribution. Figure 15 shows multiple procedurally generated clouds. The user can generate multiple clouds by controlling individual parameters and placing kernels in 3D space with their mouse to achieve any shape desired. A real-time tomography image of the generated cloud supports this process. Supplementary materials include a video of interaction with the application.



Fig. 15. Rendering of 100 randomly placed, procedurally generated clouds. In total the scene consists of 18902 Gaussian kernels and 308032 Gabor kernels. Clouds that are further back are entirely made up of Gaussian kernels. Cirrus clouds on the background are part of the environment map and not procedurally generated.

## 8 Limitations and Future Work

*Discussion on Gabor Transforms and Wavelets.* While the regression procedure delivers high quality assets, it can be slow (0.1-2h depending on the asset and mixture complexity, on a single RTX 4090) and may require some small fine tuning between assets of substantially different class. We acknowledge that a forward method, akin to discrete wavelet decompositions (DWT) and Gabor Transforms could be devised. However, Gabor kernels are not orthonormal, which generally rules them out as a valid wavelet basis; a complete frame without spectral overlap is impossible. While our work starts bridging the gap between wavelet and primitive-based rendering, we expect future work to finally enable seamless forward construction of kernel volumes without convolved regression schemes. An alternative approach for forward reconstruction could involve recent advances in Transformer-based feedforward point-based reconstruction approaches [Wang et al. 2025].

*Radiance fields.* While promising due to its similarity to cosine-modulated Gaussians, already showcased in 3DGRT [Moenne-Loccoz et al. 2024] and Gabor filter banks for 2D images [Wurster et al. 2024], and despite some concurrent work showing limited success in similar radiance-field settings [Chan et al. 2026; Zhou et al. 2025], there are fundamental limitations for using pure Gabor kernels (i.e. without a constant density base), mainly due to the view-dependence. Without dense enough training camera sampling, optimization could become tricky, as Gabor kernels might orient themselves into directions where they do not contribute to any image, appearing as artifacts after training. Regularization on the orientations, supervision on in-between frames [Hermann et al. 2025] or better pruning strategies during training may improve its chances. Nevertheless, it remains a promising direction for future work, one which could enable natural and continuous level of detail for primitive-based radiance field methods.

*Limitations of Optix Visibility Masking.* While practical when using simple decompositions, using higher numbers of orientation bins and frequency levels would require changing the way we implement them, due to the limitation of 8 possible masks. Our alternative solution using the current Optix API, used in Section 7.1, is to define some through visibility masks, and others via direct masking in the rendering kernel (i.e., avoiding integration but keeping them in the visible set). In our experiments, the biggest bottleneck remains BVH traversal and ray intersection queries, which makes this latter strategy only marginally better in terms of performance.

*Comparison to NanoVDB.* While we achieve considerable compression rates vs compressed voxel-grids (Table 4), they could be pushed even further by leveraging compression techniques such as codebook primitives, half-precision storage, and fixed frequency particles. These are orthogonal to our work and will likely trade off some performance for quality. With regards to direct comparisons in terms of render time to NanoVDB, we would like to clarify the substantial undertaking that would be implementing it efficiently in Mitsuba and DrJIT. Regardless, we consider many of the key components of Open/NanoVDB orthogonal to our work: hierarchical structuring of the primitives could in theory accelerate our rendering speed even further, and provide better scalability than visibility masks; this approach has been recently explored for 3D Gaussian Splats in the context of radiance-field rendering in fVDB [Williams et al. 2024]. Integration of our approach within fVDB is an exciting avenue of future work.

*Performance and Bias.* While we manage to generally beat Gaussians across a wide range of metrics and datasets, in some scenarios (like extreme view-dependent frequency in the "volumetrically unrealistic" edges in BUNNY) the amount of residual kernels required to uplift a low-passed Gaussian version into a high quality, high frequency feature hampers performance substantially. Also, for multiple-scattering settings, most of our acceleration strategies

rely on inducing certain amounts of bias to the render, which may not be adequate for all applications.

## 9 Conclusions

We have presented a new type of volumetric primitive fields: mixtures of Gabor and Gaussian kernels. These naturally conform continuous assets in the frequency domain sense, being tightly defined by their spectral content, and thus, kind to level of detail techniques. We have provided analytical estimators for these new kernels, and a specialized hierarchical regression technique that can progressively increase both the reference and model's frequency content. Furthermore, we have proposed a number of techniques that specifically leverage these primitive volumes to accelerate physically-based rendering, in particular exploiting angularity for the first time to significantly reduce scene traversal cost. We believe our work further connects procedural generation, wavelet volumetric approximations and primitive-based volumes, providing a path towards ever more compact and efficient physically-based rendering.

*Acknowledgements.* This project has received funding from the Swiss National Science Foundation (SNSF, Grant 200502) and an academic gift from Meta. We acknowledge access to Alps at the Swiss National Supercomputing Centre, Switzerland under USI's share (project ID u6).

## References

Antoine Bouthors and Fabrice Neyret. 2004. Modeling clouds shape. In *Eurographics (short papers)*. Eurographics Association.

Forrest B Brown and William R Martin. 2003. Direct sampling of Monte Carlo flight paths in media with continuously varying cross-sections. In *Proc. ANS Mathematics & Computation Topical Meeting*, Vol. 2.

Jiwen Chan, Zhenjun Zhao, and Yu-Lun Liu. 2026. AdaGaR: Adaptive Gabor Representation for Dynamic Scene Reconstruction. arXiv:2601.00796 [cs.CV] <https://arxiv.org/abs/2601.00796>

Subrahmanyam Chandrasekhar. 1960. *Radiative Transfer*. Courier Corporation.

Brian Chao, Hung-Yu Tseng, Lorenzo Porzi, Chen Gao, Tuotuo Li, Qinbo Li, Ayush Saraf, Jia-Bin Huang, Johannes Kopf, Gordon Wetzstein, and Changil Kim. 2025. Textured Gaussians for Enhanced 3D Scene Appearance Modeling. arXiv:2411.18625 [cs.CV] <https://arxiv.org/abs/2411.18625>

Jorge Condor, Sébastien Speierer, Lukas Bode, Aljaz Bozic, Simon Green, Piotr Didyk, and Adrian Jarabo. 2025. Don't Splat your Gaussians: Volumetric Ray-Traced Primitives for Modeling and Rendering Scattering and Emissive Media. *ACM Trans. Graph.* (month = jan 2025). doi:10.1145/3711853

Miguel Crespo, Adrian Jarabo, and Adolfo Muñoz. 2021. Primary-space adaptive control variates using piecewise-polynomial approximations. *ACM Trans. Graph.* 40, 3 (2021).

Franklin C Crow. 1984. Summed-area tables for texture mapping. In *Proceedings of the 11th annual conference on Computer graphics and interactive techniques*. 207–212.

Yoshinori Dobashi, Kazufumi Kaneda, Hideo Yamashita, Tsuyoshi Okita, and Tomoyuki Nishita. 2000. A simple, efficient method for realistic animation of clouds. In *Proceedings of the 27th annual conference on Computer graphics and interactive techniques*. 19–28.

DreamWorksAnimation. 2012–2023. OpendVDB. <https://github.com/AcademySoftwareFoundation/opendvdb>.

Andrew Edelsten, Paula Jukarainen, and Anjul Patney. 2019. Truly next-gen: Adding deep learning to games and graphics. In *In NVIDIA Sponsored Sessions (Game Developers Conference)*, Vol. 2. 7.

Marcos Fajardo and Matt Pharr. 2023. Fast Procedural Noise By Monte Carlo Sampling. doi:10.2312/sr.20231141

Marcos Fajardo, Bartłomiej Wronski, Marco Salvi, and Matt Pharr. 2023. Stochastic Texture Filtering. *arXiv preprint arXiv:2305.05810* (2023).

Julian Fong, Magnus Wrenning, Christopher Kulla, and Ralf Habel. 2017. Production volume rendering. In *ACM SIGGRAPH 2017 Courses*.

Bruno Galerne, Ares Lagae, Sylvain Lefebvre, and George Drettakis. 2012. Gabor Noise by Example. *ACM Transactions on Graphics - TOG* 31 (07 2012). doi:10.1145/2185520.2185569

Zhongpai Gao, Benjamin Planche, Meng Zheng, Anwesa Choudhuri, Terrence Chen, and Ziyan Wu. 2025. 6DGs: Enhanced Direction-Aware Gaussian Splatting for Volumetric Rendering. In *The Thirteenth International Conference on Learning Representations*. <https://openreview.net/forum?id=sUvBTEYXGt>

Geoffrey Y Gardner. 1985. Visual simulation of clouds. In *Proceedings of the 12th annual conference on Computer graphics and interactive techniques*. 297–304.

Walter Gautschi. 1970. Efficient computation of the complex error function. *SIAM J. Numer. Anal.* 7, 1 (1970), 187–198.

Iliyan Georgiev, Zackary Misro, Toshiya Hachisuka, Derek Nowrouzezahrai, Jaroslav Krivánek, and Wojciech Jarosz. 2019. Integral formulations of volumetric transmittance. *ACM Trans. Graph.* 38, 6 (2019).

Antoine Guédon and Vincent Lepetit. 2024. Sugar: Surface-aligned gaussian splatting for efficient 3d mesh reconstruction and high-quality mesh rendering. In *Proceedings of the IEEE/CVF Conference on Computer Vision and Pattern Recognition*. 5354–5363.

Brian Guenter, Mark Finch, Steven Drucker, Desney Tan, and John Snyder. 2012. Foveated 3D graphics. *ACM Transactions on Graphics* 31, 6 (2012). doi:10.1145/2366145.2366183

Stefan Guthe, Michael Wand, Julius Gonser, and Wolfgang Straßer. 2002. Interactive rendering of large volume data sets. In *IEEE Visualization, 2002. VIS 2002*. IEEE, 53–60.

Nicolai Hermann, Jorge Condor, and Piotr Didyk. 2025. Puzzle Similarity: A Perceptually-guided Cross-Reference Metric for Artifact Detection in 3D Scene Reconstructions. In *Proceedings of the IEEE/CVF International Conference on Computer Vision (ICCV)*. 28881–28891.

Wenzel Jakob, Sébastien Speierer, Nicolas Roussel, Merlin Nimier-David, Delio Vicini, Tizian Zeltner, Baptiste Nicolet, Miguel Crespo, Vincent Leroy, and Ziyi Zhang. 2022. *Mitsuba 3 renderer*. <https://mitsuba-renderer.org>.

Simon Kallweit, Thomas Müller, Brian Mcwilliams, Markus Gross, and Jan Novák. 2017. Deep Scattering: Rendering Atmospheric Clouds with Radiance-Predicting Neural Networks. *ACM Trans. Graph.* 36, 6 (2017).

Volodymyr Karpenko, Taimoor Tariq, Jorge Condor, and Piotr Didyk. 2025. Human Vision Constrained Super-Resolution. In *Proceedings of the IEEE/CVF International Conference on Computer Vision*. 4742–4751.

Nikhil Keetha, Jay Karhade, Krishna Murthy Jatavallabhula, Gengshan Yang, Sebastian Scherer, Deva Ramanan, and Jonathon Luiten. 2024. Splatam: Splat track & map 3d gaussians for dense rgb-d slam. In *Proceedings of the IEEE/CVF Conference on Computer Vision and Pattern Recognition*. 21357–21366.

Bernhard Kerbl, Georgios Kopanas, Thomas Leimkühler, and George Drettakis. 2023. 3D Gaussian Splatting for Real-Time Radiance Field Rendering. *ACM Trans. Graph.* 42, 4 (2023).

Bernhard Kerbl, Andréas Meuleman, Georgios Kopanas, Michael Wimmer, Alexandre Lanvin, and George Drettakis. 2024. A Hierarchical 3D Gaussian Representation for Real-Time Rendering of Very Large Datasets. arXiv:2406.12080 [cs.CV] <https://arxiv.org/abs/2406.12080>

Markus Kettunen, Eugene D'Eon, Jacopo Pantaleoni, and Jan Novák. 2021. An unbiased ray-marching transmittance estimator. *ACM Trans. Graph.* 40, 4 (2021).

Shakiba Kheradmand, Daniel Rebain, Gopal Sharma, Weiwei Sun, Yang-Che Tseng, Hossam Isack, Abhishek Kar, Andrea Tagliasacchi, and Kwang Moo Yi. 2024. 3D Gaussian Splatting as Markov Chain Monte Carlo. In *Advances in Neural Information Processing Systems (NeurIPS)*. Spotlight Presentation.

Doyub Kim, Minjae Lee, and Ken Museth. 2024. NeuralVDB: High-resolution Sparse Volume Representation using Hierarchical Neural Networks. *ACM Trans. Graph.* 43, 2 (2024).

Diederik P. Kingma and Jimmy Ba. 2014. Adam: A Method for Stochastic Optimization. *CoRR* abs/1412.6980 (2014). <https://api.semanticscholar.org/CorpusID:6628106>

Aaron Knoll, Gregory P. Johnson, and Johannes Meng. 2021. Path Tracing RBF Particle Volumes. In *Ray Tracing Gems II*, Adam Marrs, Peter Shirley, and Ingo Wald (Eds.). Apress.

Soheil Kolouri, Kimia Nadjahi, Umut Simsekli, Roland Badeau, and Gustavo Rohde. 2019. Generalized sliced wasserstein distances. *Advances in neural information processing systems* 32 (2019).

Ares Lagae, Sylvain Lefebvre, George Drettakis, and Philip Dutré. 2009. Procedural noise using sparse Gabor convolution. *ACM Transactions on Graphics (TOG)* 28, 3 (2009), 1–10.

Christoph Lassner and Michael Zollhofer. 2021. Pulsar: Efficient sphere-based neural rendering. In *Proceedings of the IEEE/CVF conference on computer vision and pattern recognition*. 1440–1449.

David Laur and Pat Hanrahan. 1991. Hierarchical splatting: A progressive refinement algorithm for volume rendering. *ACM SIGGRAPH computer graphics* 25, 4 (1991), 285–288.

Stephen Lombardi, Tomas Simon, Gabriel Schwartz, Michael Zollhofer, Yaser Sheikh, and Jason Saragih. 2021. Mixture of Volumetric Primitives for Efficient Neural Rendering. *ACM Trans. Graph.* 40, 4 (2021).

Guillaume Loubet and Fabrice Neyret. 2017. Hybrid mesh-volume LoDs for all-scale pre-filtering of complex 3D assets. *Computer Graphics Forum* 36, 2 (2017), 431–442. arXiv:<https://onlinelibrary.wiley.com/doi/10.1111/cgf.13138> doi:10.1111/cgf.13138

13138

David Luebke, Martin Reddy, Jonathan D Cohen, Amitabh Varshney, Benjamin Watson, and Robert Huebner. 2002. *Level of detail for 3D graphics*. Elsevier.

S Marćelja. 1980. Mathematical description of the responses of simple cortical cells. *Journal of the Optical society of America* 70, 11 (1980), 1297–1300.

Nelson L Max. 1979. ATOMILL: ATOMS with shading and highlights. *ACM SIGGRAPH Computer Graphics* 13, 2 (1979).

Johannes Meng, Marios Papas, Ralf Habel, Carsten Dachsbacher, Steve Marschner, Markus Gross, and Wojciech Jarosz. 2015. Multi-Scale Modeling and Rendering of Granular Materials. *ACM Trans. Graph.* 34, 4 (2015).

Ben Mildenhall, Pratul P. Srinivasan, Matthew Tancik, Jonathan T. Barron, Ravi Ramamoorthi, and Ren Ng. 2020. NeRF: Representing Scenes as Neural Radiance Fields for View Synthesis. In *Proceedings of ECCV*.

Nicolas Moenne-Loccoz, Ashkan Mirzaei, Or Perel, Riccardo de Lutio, Janick Martinez Esturo, Gavriel State, Sanja Fidler, Nicholas Sharp, and Zan Gojcic. 2024. 3D Gaussian Ray Tracing: Fast Tracing of Particle Scenes. *ACM Trans. Graph.* 43, 6, Article 232 (Nov. 2024), 19 pages. doi:10.1145/3687934

Bipul Mohanto, ABM Tarique Islam, Enrico Gobbetti, and Oliver Staadt. 2022. An Integrative View of Foveated Rendering. *Computers & Graphics* 102 (2022), 474–501. doi:doi.org/10.1016/j.cag.2021.10.010

Jonathan T. Moon, Bruce Walter, and Stephen R. Marschner. 2007. Rendering Discrete Random Media Using Precomputed Scattering Solutions. In *Proceedings of EGSR*.

Thomas Müller, Alex Evans, Christoph Schied, and Alexander Keller. 2022. Instant Neural Graphics Primitives with a Multiresolution Hash Encoding. *ACM Trans. Graph.* 41, 4 (2022).

Ken Museth. 2013a. VDB: High-resolution sparse volumes with dynamic topology. *ACM Trans. Graph.* 32, 3 (2013).

Ken Museth. 2013b. VDB: High-resolution sparse volumes with dynamic topology. *ACM transactions on graphics (TOG)* 32, 3 (2013), 1–22.

Ken Museth. 2021a. NanoVDB: A GPU-friendly and portable VDB data structure for real-time rendering and simulation. In *ACM SIGGRAPH 2021 Talks*.

Ken Museth. 2021b. NanoVDB: A GPU-friendly and portable VDB data structure for real-time rendering and simulation. In *ACM SIGGRAPH 2021 Talks*. 1–2.

Fabrice Neyret. 1998. Modeling, Animating, and Rendering Complex Scenes Using Volumetric Textures. *IEEE Trans. Vis. Comput. Graph.* 4, 1 (1998).

Jan Novák, Iliyan Georgiev, Johannes Hanika, and Wojciech Jarosz. 2018. Monte Carlo methods for volumetric light transport simulation. *Computer Graphics Forum* 37, 2 (2018).

Jan Novák, Andrew Selle, and Wojciech Jarosz. 2014. Residual ratio tracking for estimating attenuation in participating media. *ACM Trans. Graph.* 33, 6 (2014).

Lena Petrovic, Mark Henne, and John Anderson. 2005. Volumetric methods for simulation and rendering of hair. *Pixar Animation Studios* 2, 4 (2005).

Gert PM Poppe and Christianus MJ Wijers. 1990. More efficient computation of the complex error function. *ACM Transactions on Mathematical Software (TOMS)* 16, 1 (1990), 38–46.

Christian Reiser, Songyou Peng, Yiyi Liao, and Andreas Geiger. 2021. KiloNeRF: Speeding up Neural Radiance Fields with Thousands of Tiny MLPs. In *Proceedings of ICCV*.

Kai Schröder, Reinhard Klein, and Arno Zinke. 2011. A Volumetric Approach to Predictive Rendering of Fabrics. *Computer Graphics Forum* 30, 4 (2011).

Eero P Simoncelli and William T Freeman. 1995. The steerable pyramid: A flexible architecture for multi-scale derivative computation. In *Proceedings of International Conference on Image Processing*. Vol. 3. IEEE, 444–447.

Eero P Simoncelli, William T Freeman, Edward H Adelson, and David J Heeger. 1992. Shiftable multiscale transforms. *IEEE transactions on Information Theory* 38, 2 (1992), 587–607.

Hans Strasburger, Ingo Rentschler, and Martin Jüttner. 2011. Peripheral vision and pattern recognition: A review. *Journal of Vision* 11, 5 (12 2011). doi:10.1167/11.5.13

Luca Surace, Marek Wernikowski, Cara Tursun, Karol Myszkowski, Radosław Mantiuk, and Piotr Didyk. 2023. Learning GAN-Based Foveated Reconstruction to Recover Perceptually Important Image Features. *ACM Transactions on Applied Perception* 20, 2 (2023). doi:10.1145/3583072

László Szirmay-Kalos, Iliyan Georgiev, Milán Magdics, Balázs Molnár, and Dávid Légrády. 2017. Unbiased light transport estimators for inhomogeneous participating media. *Computer Graphics Forum* 36, 2 (2017).

Heang K Tuy and Lee Tat Tuy. 1984. Direct 2-D display of 3-D objects. *IEEE Computer Graphics and Applications* 4, 10 (1984).

Jianyuan Wang, Minghai Chen, Nikita Karaev, Andrea Vedaldi, Christian Rupprecht, and David Novotny. 2025. Vggt: Visual geometry grounded transformer. In *Proceedings of the Computer Vision and Pattern Recognition Conference*. 5294–5306.

Zhou Wang, A.C. Bovik, H.R. Sheikh, and E.P. Simoncelli. 2004. Image quality assessment: from error visibility to structural similarity. *IEEE Transactions on Image Processing* 13, 4 (2004).

Manfred Weiler, Rüdiger Westermann, Chuck Hansen, Kurt Zimmermann, and Thomas Ertl. 2000. Level-of-detail volume rendering via 3D textures. In *Proceedings of the 2000 IEEE symposium on Volume visualization*. 7–13.

Francis Williams, Jiahui Huang, Jonathan Swartz, Gergely Klar, Vijay Thakkar, Matthew Cong, Xuanchi Ren, Ruilong Li, Clement Fuji-Tsang, Sanja Fidler, Eftychios Sifakis, and Ken Museth. 2024. fVDB: A Deep-Learning Framework for Sparse, Large Scale, and High Performance Spatial Intelligence. *ACM Transactions on Graphics* 43, 4 (2024). doi:10.1145/3658226

Felix Windisch, Thomas Köhler, Lukas Radl, Michael Steiner, Dieter Schmalstieg, and Markus Steinberger. 2025. A LoD of Gaussians: Unified Training and Rendering for Ultra-Large Scale Reconstruction with External Memory. arXiv:2507.01110 [cs.GR] <https://arxiv.org/abs/2507.01110>

E Woodcock. 1965. Techniques used in the GEM code for Monte Carlo neutronics calculations in reactors and other systems of complex geometry. In *Proceedings of the Conference on Applications of Computing Methods to Reactor Problems*, Vol. 557.

Magnus Wrenninge, Nafees Bin Zafar, O Harding, G Graham, J Tessendorf, V Grant, A Clinton, and A Bouthors. 2011. Production volume rendering. *ACM SIGGRAPH Course notes*.

Guanjun Wu, Taoran Yi, Jiemin Fang, Lingxi Xie, Xiaopeng Zhang, Wei Wei, Wenyu Liu, Qi Tian, and Xinggang Wang. 2024. 4d gaussian splatting for real-time dynamic scene rendering. In *Proceedings of the IEEE/CVF conference on computer vision and pattern recognition*. 20310–20320.

Wei Wu and Greg M McFarquhar. 2018. Statistical theory on the functional form of cloud particle size distributions. *Journal of the Atmospheric Sciences* 75, 8 (2018), 2801–2814.

Skylar Wurster, Ran Zhang, and Changxi Zheng. 2024. Gabor Splatting for High-Quality Gigapixel Image Representations. In *ACM SIGGRAPH 2024 Posters* (Denver, CO, USA) (SIGGRAPH '24). Association for Computing Machinery, New York, NY, USA, Article 66, 2 pages. doi:10.1145/3641234.3671081

Xijie Yang, Lining Xu, Lihuan Jiang, Dahua Lin, and Bo Dai. 2025. Virtualized 3D Gaussians: Flexible Cluster-based Level-of-Detail System for Real-Time Rendering of Composed Scenes. In *Proceedings of the Special Interest Group on Computer Graphics and Interactive Techniques Conference Papers (SIGGRAPH Conference Papers '25)*. ACM, 1–11. doi:10.1145/3721238.3730602

Mofreh R. Zaghloul and Ahmed N. Ali. 2012. Algorithm 916: Computing the Faddeyeva and Voigt Functions. *ACM Trans. Math. Softw.* 38, 2, Article 15 (Jan. 2012), 22 pages. doi:10.1145/2049673.2049679

Shuang Zhao, Wenzel Jakob, Steve Marschner, and Kavita Bala. 2011. Building Volumetric Appearance Models of Fabric Using Micro CT Imaging. *ACM Trans. Graph.* 30, 4 (2011).

Junyu Zhou, Yuyang Huang, Wenrui Dai, Junni Zou, Ziyang Zheng, Nuowen Kan, Chenglin Li, and Hongkai Xiong. 2025. 3DGabSplat: 3D Gabor Splatting for Frequency-adaptive Radiance Field Rendering. arXiv:2508.05343 [cs.CV] <https://arxiv.org/abs/2508.05343>

## 10 Deriving Analytical Line Integrals of the 3D Anisotropic Gabor Kernel

Here we present the step-by-step derivation of the closed-form definite line integrals for the 3D anisotropic Gabor kernel along an arbitrary ray. Following the Gabor kernel defined in Eq. (6),

*Kernel definition.* Recall that

$$g(x; \mu, \Sigma, \omega) = \frac{1}{\sqrt{8\pi^3 |\Sigma|}} \exp\left(-\frac{1}{2}(x - \mu)^T \Sigma^{-1} (x - \mu)\right) \cos(\vec{\omega}^T (x - \mu)). \quad (35)$$

Defining the effective modulation vector

$$\vec{\omega} \equiv RS^{-1}(\omega, \omega, \omega), \quad (36)$$

*Line parameterization.* Let the line be parameterized as

$$x(t) = p_0 + \vec{v}t, \quad t \in [t_0, t_1], \quad (37)$$

and define the offset

$$d = p_0 - \mu. \quad (38)$$

The line integral is

$$I = \int_{t_0}^{t_1} g(x(t)) dt. \quad (39)$$

10.0.1 *Reduction to a 1D Integral.* Substituting the line parameterization,

$$I = \frac{1}{\sqrt{8\pi^3|\Sigma|}} \int_{t_0}^{t_1} \exp\left(-\frac{1}{2}(d+tv)^T \Sigma^{-1}(d+tv)\right) \cos(\vec{\omega}^T(d+tv)) dt. \quad (40)$$

Introduce the scalar quantities, resulting from partial whitening of the space (only translation and rotation to local coordinates for better clarity)

$$a = v^T \Sigma^{-1} v, \quad (41)$$

$$\beta = v^T \Sigma^{-1} d, \quad (42)$$

$$\gamma = d^T \Sigma^{-1} d, \quad (43)$$

$$B = \vec{\omega}^T v, \quad (44)$$

$$\delta = \vec{\omega}^T d. \quad (45)$$

Then

$$(d+tv)^T \Sigma^{-1}(d+tv) = at^2 + 2\beta t + \gamma, \quad (46)$$

$$\vec{\omega}^T(d+tv) = Bt + \delta. \quad (47)$$

Thus,

$$I = \frac{1}{\sqrt{8\pi^3|\Sigma|}} \int_{t_0}^{t_1} \exp\left(-\frac{1}{2}(at^2 + 2\beta t + \gamma)\right) \cos(Bt + \delta) dt. \quad (48)$$

—

10.0.2 *Complex Exponential Form.* Using Euler's formula, we can transform the cosine as  $\cos \theta = \Re(e^{i\theta})$ ,

$$I = \frac{1}{\sqrt{8\pi^3|\Sigma|}} \Re\left\{e^{i\delta} e^{-\frac{1}{2}\gamma} \int_{t_0}^{t_1} \exp\left(-\frac{1}{2}at^2 - \beta t + iBt\right) dt\right\}. \quad (49)$$

Completing the square,

$$-\frac{1}{2}at^2 - \beta t + iBt = -\frac{1}{2}a\left(t - \frac{-\beta + iB}{a}\right)^2 + \frac{(-\beta + iB)^2}{2a}. \quad (50)$$

—

10.0.3 *Finite-Domain Closed Form.* Define

$$\alpha = \sqrt{\frac{a}{2}}, \quad \zeta = \frac{-\beta + iB}{\sqrt{2a}}. \quad (51)$$

The finite-domain integral evaluates to

$$I = \frac{1}{\sqrt{8\pi^3|\Sigma|}} \Re\left\{e^{i\delta} e^{-\frac{1}{2}\gamma} \sqrt{\frac{\pi}{2a}} \exp\left(\frac{(-\beta + iB)^2}{2a}\right) \times [\operatorname{erf}(\alpha t_1 - \zeta) - \operatorname{erf}(\alpha t_0 - \zeta)]\right\}. \quad (52)$$

This expression is exact and valid for any finite ray segment.

—

10.0.4 *Infinite-Domain Limit.* Taking the limits  $t_0 \rightarrow -\infty, t_1 \rightarrow +\infty$  and using  $\operatorname{erf}(\pm\infty) = \pm 1$ , we obtain

$$I_\infty = \frac{1}{\sqrt{8\pi^3|\Sigma|}} \sqrt{\frac{2\pi}{a}} \exp\left(-\frac{1}{2}\left(\gamma - \frac{\beta^2}{a}\right)\right) \exp\left(-\frac{B^2}{2a}\right) \cos\left(\delta - \frac{\beta B}{a}\right). \quad (53)$$

In a fully whitened space (including scale), the expression simplifies by turning  $a = 1$ , and multiplying by the corresponding length scalar to compensate for the space compression, rendering  $\mathcal{K}$  as defined in Section 4.

## 11 Frequency and Orientation Sampling Strategies

We include a number of stochastic-analytic estimators in Tables 5 and 6.

## 12 Analytic Fourier Transform for Gabor Kernels

Recalling again that the Gabor kernel is defined as a Gaussian modulated by a cosine function:

$$\mathcal{G}(x; \mu, \Sigma, \omega) = \frac{1}{\sqrt{8\pi^3|\Sigma|}} e^{-\frac{1}{2}(x-\mu)^T \Sigma^{-1}(x-\mu)} \cos(\vec{\omega}^T(x-\mu)) \quad (54)$$

In our experiments, we redefine  $\vec{\omega}$  with a scalar  $\omega$ , but for the derivation, without loss of generalization, we use  $\vec{\omega}$  as an arbitrary orientation of the modulation. We derive the analytic continuous Fourier Transform of the Gabor kernel using angular frequencies  $k = 2\pi\xi$ . We define  $y = x - \mu$  and use the shift theorem to shift to zero mean.

$$\mathcal{F}\{\mathcal{G}(x)\}(k) = e^{-ik^T \mu} \mathcal{F}\{f(y)\}(k) \quad (55)$$

where

$$f(y) = \frac{1}{\sqrt{8\pi^3|\Sigma|}} e^{-\frac{1}{2}y^T \Sigma^{-1}y} \cos(\vec{\omega}^T y) \quad (56)$$

Using Euler's formula

$$\cos(b^T y) = \frac{1}{2} [e^{i\vec{\omega}^T y} + e^{-i\vec{\omega}^T y}] \quad (57)$$

and applying the frequency-shifting property

$$\mathcal{F}\{h(y)e^{i\vec{\omega}^T y}\}(k) = \mathcal{F}\{h(y)\}(k - \vec{\omega}) \quad (58)$$

twice, we obtain by linearity

$$\mathcal{F}\{f(y)\}(k) = \frac{1}{2} [\mathcal{F}\{h(y)\}(k - \vec{\omega}) + \mathcal{F}\{h(y)\}(k + \vec{\omega})] \quad (59)$$

where

$$h(y) = \frac{1}{\sqrt{8\pi^3|\Sigma|}} e^{-\frac{1}{2}y^T \Sigma^{-1}y} \quad (60)$$

and

$$\mathcal{F}\{h(y)\}(k) = e^{-\frac{1}{2}k^T \Sigma k} \quad (61)$$

Putting everything together, we conclude with the final form

$$\mathcal{F}\{\mathcal{G}(x)\}(k) = \frac{1}{2} e^{-ik^T \mu} \left[ e^{-\frac{1}{2}(k-\vec{\omega})^T \Sigma (k-\vec{\omega})} + e^{-\frac{1}{2}(k+\vec{\omega})^T \Sigma (k+\vec{\omega})} \right] \quad (62)$$

Lastly, we show how to convert between our continuous, angular frequency definition and Discrete Fourier Transforms (DFT) in cycles as computed by most FFT packages. Cycles and radians are related by  $k = 2\pi\xi$ , thus  $F_{\text{cont}}(k) = F_{\text{cont}}(2\pi\xi)$ . Then we discretize our continuous function by approximating it with a Riemann sum over

Table 5. Stochastic sampling strategies across frequency levels, with  $\mathcal{P}$  being the number of levels in the pyramid,  $\beta$  the power law shape parameter and  $a, b$  the limits on the segment bucket the sample fell into (e.g. in a pyramid with  $\mathcal{P} = 4$ , the first level would have  $a = 0, b = \frac{1}{4}$ ). In control variate modes, Gaussians (i.e. zero-frequency Gabor kernels) have a weight of 1.

Strategy	Description	Sampling Function $f(x)$	Sampling Weight (Reciprocal Probability)
Deterministic	Renders all frequency levels (no sampling).	—	1
Uniform Sampling	Samples frequency levels uniformly.	$\mathcal{P}^{-1}$	$\frac{1}{\mathcal{P}}$
Power-law Weighted	Samples proportionally to a tuned power-law function.	$x^{(1-\beta)^{-1}}$	$\left(b^{(1-\beta)} - a^{(1-\beta)}\right)^{-1}$
Uniform + Control Variate	Gaussians as a control variate; samples remaining levels uniformly.	$(\mathcal{P} - 1)^{-1}$	$\frac{1}{\mathcal{P} - 1}$
Power-law + Control Variate	Gaussians as a control variate; others sampled via power-law.	$x^{(1-\beta)^{-1}}$	$\left(b^{(1-\beta)} - a^{(1-\beta)}\right)^{-1}$
Power-law + CV (Accum.)	Samples level $k$ via power-law; renders all levels 0 to $k$ .	$x^{(1-\beta)^{-1}}$	$\left(1 - \left(\frac{j}{\mathcal{P}}\right)^{1-\beta}\right)^{-1}$

Table 6. Orientation-selective sampling strategies for steerable pyramid rendering, with  $K$  being the number of orientation bins,  $\gamma$  the decay rate parameter,  $a_i = |\vec{v} \cdot \mathbf{o}_i|$  the alignment between ray direction  $\vec{v}$  and orientation bin  $\mathbf{o}_i$ , and  $\delta$  the alignment threshold. The contribution weight is  $w_i = \exp(-f_0^2 a_i^2 / 2)$ , with  $W = \sum_{i=1}^K w_i$ . For deterministic threshold culling, we can simply tune "aggressiveness" in the form of the factor  $\delta$ ; this allows us to sacrifice quality for performance in a direct manner, as lower thresholds result in more aggressive dropping of orientation bins, eventually degenerating into simply integrating the highest contributing one. Volumes with high  $f_0$  will benefit from such a setting due to their high orientation selectivity, for example.

Strategy	Description	Sampling Probability	Sampling Weight
Deterministic	Renders all orientation bins (no culling).	—	1
Threshold Culling	Renders bins with $a_i \leq \delta$ (perpendicular enough).	—	1
Uniform Sampling	Uniformly samples one orientation bin.	$K^{-1}$	$K$
Importance Sampling	Samples bins proportionally to contribution weight.	$\frac{w_i}{W}$	$\frac{W}{w_i}$
Threshold + Uniform	Renders all bins with $a_i \leq \delta$ ; uniformly samples one with $a_i > \delta$ .	$N_{\text{above}}^{-1}$	$N_{\text{above}}$

Note: In Threshold + Control Variate mode, below-threshold bins have weight 1, and  $N_{\text{above}}$  is the per-ray count of bins with  $a_i > \delta$ .

a discrete grid  $V \in \mathbb{R}^{N_x \times N_y \times N_z}$  and a physical domain  $[a, b]^3$  with  $a, b \in \mathbb{R}$  and a uniform sample spacing of  $\Delta V = \Delta x \Delta y \Delta z = \frac{(b-a)^3}{N_x N_y N_z}$ :

$$\int_{[a,b]^3} f(\mathbf{r}) e^{-2\pi i \xi^T \mathbf{r}} d\mathbf{r} \approx \Delta V \sum_{n=0}^{N_x-1} \sum_{m=0}^{N_y-1} \sum_{l=0}^{N_z-1} f(\mathbf{r}_{n,m,l}) e^{-2\pi i \xi^T \mathbf{r}_{n,m,l}} \quad (63)$$

The 3D DFT is unnormalized and defined as:

$$F_{\text{DFT}}[p, q, r] = \sum_{n=0}^{N_x-1} \sum_{m=0}^{N_y-1} \sum_{l=0}^{N_z-1} f(\mathbf{r}_{n,m,l}) e^{-2\pi i (\frac{pn}{N_x} + \frac{qm}{N_y} + \frac{rl}{N_z})} \quad (64)$$

thus

$$\xi^T \mathbf{r}_{n,m,l} = \frac{pn}{N_x} + \frac{qm}{N_y} + \frac{rl}{N_z} \quad (65)$$

yields

$$F_{\text{cont}}(2\pi\xi) \approx \Delta V F_{\text{DFT}}[p, q, r] \quad (66)$$

which we solve for  $F_{\text{DFT}}$ :

$$F_{\text{DFT}}[p, q, r] = \frac{1}{\Delta V} F_{\text{cont}}(k_x = 2\pi\xi_p, k_y = 2\pi\xi_q, k_z = 2\pi\xi_r) \quad (67)$$

with  $\xi_p = \frac{p}{N_x \Delta x}$  and  $p = 0, \dots, N_x - 1$ , and similarly for  $\xi_q$  and  $\xi_r$ .

### 13 Optimization Hyperparameters

In Table 7, we summarize the hyperparameters used to regress all assets presented in this work.

Table 7. Resulting optimization parameters after conducting hyperparameter searches.

Parameter	Learning Rate
<i>Parameter-specific Learning Rates</i>	
Centers $\mu$	0.012
Scales $s$	0.0008
Quaternions $q$	0.0012
Weight $\alpha$	0.00008
Omega $\omega$	0.002
<i>Regularization &amp; Control</i>	
$\lambda_\alpha$	0.00001
$\lambda_s$	0.02
$\lambda_{\text{noise}}$	250
$\gamma$	0.65
<i>Optimization Schedule</i>	
Warmup ratio	0.15
Min LR ratio	0.1
Iterations (Gaussian)	300
Iterations (Gabor)	300
<i>Densification &amp; Pruning</i>	
Resample Primitives	every 30 it
Resample until	210 it